Sustainable Materials and Technologies 42 (2024) e01123

Contents lists available at ScienceDirect

Sustainable Materials and Technologies

journal homepage: www.elsevier.com/locate/susmat

Sodium thiosulfate modified graphitic carbon nitride for enhancing the photocatalytic production of aldehydes

M. Alejandra Quintana, Julia Aguirre, M. Ángeles Martín-Lara, Mónica Calero, Mario J. Muñoz-Batista *, Rafael R. Solís *

Department of Chemical Engineering, University of Granada, Avda. Fuentenueva s/n, 18071 Granada, Spain

ARTICLE INFO

Keywords:
Graphitic carbon nitride
Thiosulfate
Photocatalytic oxidation
Aldehydes
Selectivity

ABSTRACT

The oxidation of alcohols to aldehydes is one of the most relevant reactions in organic chemistry. The currently implemented methods based on expensive noble metallic catalysts, toxic solvents, and high temperature and pressure conditions have released the seek for softer and cheaper alternatives such as photocatalysis. In this sense, graphitic carbon nitride has been modified with sodium thiosulfate as a source of S and Na^+ incorporation in the structure, aimed at enhancing the photocatalytic performance on the oxidation of alcohols to aldehydes, i.e. cinnamaldehyde, benzaldehyde, and vanillin in aqueous solution. Three g-C_3N_4 samples synthesized from different precursors, i.e. melamine, thiourea, and urea, were treated with sodium thiosulfate. Urea led to the g-C_3N_4 with the highest mesoporosity (surface area, 69 $m^2\ g^{-1}$) and photocatalytic activity. The modification with 5 % (wt.) of $Na_2S_2O_3$ enhanced the pseudo-first order rate constant of cinnamyl alcohol oxidation from 0.265 h^{-1} (bare sample) to 0.792 h^{-1} ($Na_2S_2O_3$-modified). The characterization of the material suggests a better charge separation of the photogenerated charges after S and Na^+ incorporation in the structure, minimizing the recombination rate of photogenerated charges. The optimum photocatalyst, tested in aqueous solution, was most selective in the production of benzaldehyde (selectivity, >100 %) > cinnamaldehyde (>23 %) > vanillin (~5 %). The selectivity was considerably boosted under acetonitrile as the solvent medium, raising in the case of cinnamaldehyde the 23 % recorded in water to 51 % in pure acetonitrile. The degradation mechanism suggests a strong influence of the photogenerated holes and the superoxide radical, the latter being more selective in the oxidation of the alcohol.

1. Introduction

The production of ketones, aldehydes, and carboxylic acids from the oxidation of alcohols is one of the paramount reactions in industrial organic chemistry [1,2]. Cinnamaldehyde has uncountable applications in the food industry [3] and recently its pharmacological activity has been valued [4,5]. Benzaldehyde is a raw material with ample applications in the fields of medicine, chemical industry, printing, and dyeing [6]. Vanillin has traditionally been used in the food industry as an additive due to its flavor and antimicrobial activity [7]. In addition, the role played by vanillin in the cosmetics and perfumes area is relevant [8]. Moreover, it has been stated as an emerging intermediate in the synthesis of pharmaceutical products [9] or even as a therapeutic molecule [10].

The oxidation of aromatic alcohols to aldehydes has been implemented using traditional oxidants such as ozone, peroxides, or halides, or under catalytic scenarios considering metal oxides, noble metals, and metal-free catalysts. Nevertheless, the required operation conditions under high temperature and pressure raise the cost and complexity. In this sense, photocatalysis emerges as a green novel technology to promote certain synthetic pathways that selectively trigger the formation of some added-value chemicals [11,12]. From all the tested photocatalysts to date, TiO_2 stands out by far [13]. However, some free-metals photocatalysts are acquiring relevance such as graphitic carbon nitride (g-C_3N_4) [14], an organocatalyst with semiconductor properties featured by polymeric melon laminates with a bandgap of 2.7 eV, i.e. photoactivation up to 460 nm [15]. g-C_3N_4 is prepared from the thermal polymerization of nitrogen-enriched precursors. However, the resultant g-C_3N_4 may display excessive aggregation of laminates that result in limited surface area, reactive sites, and limited visible light harvesting, both negative for the photocatalytic application [16]. This drawback can be alleviated by selecting an adequate precursor [17]. The use of sodium

* Corresponding authors.
E-mail addresses: mariomunoz@ugr.es (M.J. Muñoz-Batista), rafarsolis@ugr.es (R.R. Solís).

https://doi.org/10.1016/j.susmat.2024.e01123
Received 4 August 2024; Received in revised form 12 September 2024; Accepted 19 September 2024
Available online 19 September 2024

thiosulfate as a sulfur-containing precursor has been widely implemented in sulfur doping of carbon-based materials. Sodium thiosulfate decomposes under thermal treatment, triggering the release of sulfur species that react with the carbon nitride structure [18]. Nonetheless, the use of thiosulfate in graphitic carbon nitride is quite limited. It has been used as a sulfur precursor to generate the deposition of elemental sulfur nanoparticles after modification with citric and ascorbic acid [19], enlarging the radiation absorption in the visible region, and improving the reduction of Cr^{6+} to Cr^{3+}. In other work, the carbon nitride has been modified under an aqueous solution of $Na_2S_2O_3$, aimed at creating some nitrogen vacancies and acting as potential reactive sites. Hence, the presence of these irregularities in the structure modulates the formation of $HO^{\bullet}$ in the photocatalytic degradation of fluoroquinolones [20].

Based on the lack of information on the use of thiosulfate as a plausible modifier of g-C_3N_4, this work aims to study this strategy for the enhancement of the photocatalytic properties of g-C_3N_4 oriented to improve the photocatalytic transformation of alcohols to aldehydes in aqueous solution. The influence of three different g-C_3N_4 precursors, i.e. melamine, thiourea, and urea, has been selected to prepare the bare g-C_3N_4 formula. In a second step, a $Na_2S_2O_3$ modification of the g-C_3N_4 samples obtained has been studied, urea being the most convenient and the one that largest boosted the kinetics of the oxidation of cinnamyl alcohol after thiosulfate modification. The ratio thiosulfate: g-C_3N_4 has been explored in the range of 1–10 %, with an optimum value centered at 5 %. The optimum sample was also tested in acetonitrile and water with other alcohols such as benzyl alcohol and vanillyl alcohol.

2. Experimental section

2.1. Materials and synthesis of S-modified g-C_3N_4

All the chemicals were acquired from Merck®, analytical grade at least, and were used as received. For chromatographic analysis, acetonitrile of HPLC grade was used. The solutions were made with ultrapure water from a Direct-Q®-UV purification system (18.2 MΩ cm, Millipore®).

The synthesis of graphitic carbon nitride (CN) was conducted by thermal polymerization of different precursors (>99 %), i.e. melamine, urea, and thiourea, by setting a certain amount in a covered ceramic crucible at 550 °C (heating rate, 10 °C min^{-1}) for 2 h. The resulting materials were labeled as CNx where 'x' stands for the precursor used, i.e. melamine (CNm), urea (CNu), and thiourea (CNt). The sulfur-modification of these carbon nitride materials (SCNx) was carried out in a second stage, as depicted in Fig. 1. Then, $Na_2S_2O_3$ (1–10 % wt. to the CN amount) was mixed with the CNx and ground in a mortar. The resulting mixture was then thermally treated under N_2 atmosphere (100 mL min^{-1}) at 550 °C (heating rate, 10 °C min^{-1}) for 2 h. The obtained solid was crushed and labeled as SCNx-y% where 'y' stands for the S doping percentage (wt%).

2.2. Characterization of the S-modified g-C_3N_4 samples

The thermal behavior of the precursors during the polymerization to g-C_3N_4 was analyzed using a thermobalance STA 6000 from Perkin Elmer®. The sample was heated from room temperature to 850 °C (heating rate, 20 °C min^{-1}) under N_2 flow (20 mL min^{-1}).

The crystal properties were analyzed by X-ray diffraction (XRD). The diffractometer used was a Bruker D8 Discover, coupled to a Pilatus 3R 100 K-A detector, working with Cu Kα radiation (1.5406 Å). The diffractograms were registered in the 2θ range of 5–65° (monitoring rate, 0.034° min^{-1}). The crystallite size ($L_{crystal}$) and the interlayer spacing (d_{layer}) were calculated with the help of the freeware QualX® to process the data [21]. The relation $L_{crystal}/d_{layer}$ was considered a tentative approach to quantify the number of layers [22]. The structural properties were further evaluated by Fourier Transform InfraRed (FTIR) Spectroscopy, conducted in a Perkin Elmer FTIR device, model Spectrum 65. The FTIR spectra were recorded in the interval 550–4000 cm^{-1}. Adsorption-desorption isotherms with N_2 at 77 K were conducted to assess the textural properties. The samples were first degassed under vacuum at 110 °C, in a prep J4 station from 3P Instruments©. Next, the isotherms were obtained in a Sync 200 physisorption device of 3P Instruments©. The total specific surface area was calculated by the standardized Brunauer-Emmett-Teller method (S_{BET}), and the N_2 uptake at $p/p_0 \sim 0.99$ was referenced for calculating the total specific pore volume (V_T).

The elemental composition was determined in a Flash 2000 device of CHNS analyzer from ThermoScientific™. The surface chemical environment was assessed by X-ray Photoelectron Spectroscopy (XPS). The device used was a Kratos AXIS UltraDLD, operating with an X-ray source from Al Kα. The recorded spectra were referenced to the C_{1s} peak of adventitious carbon at 284.6 eV. The data was processed with the aid of the software XPSpeak 4.1®, and a Shirley background correction was applied as background.

The morphological properties were examined through Scan Transmission Electron Microscopy (STEM) in a Thermo Fisher Scientific

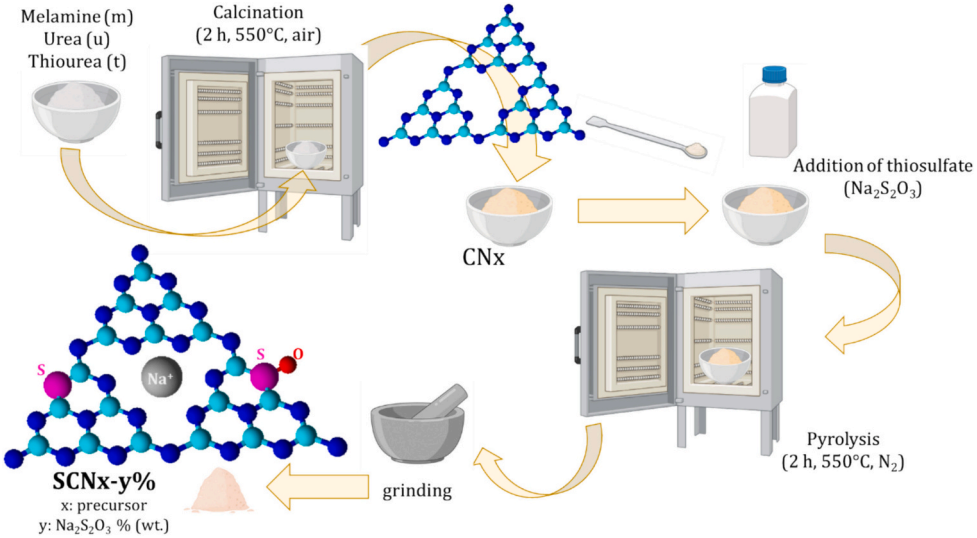

Fig. 1. Synthesis process of the thiosulfate-modified g-C_3N_4 samples.

TALOS F200X G2device (20-200 kV) equipped with High-Angle Annular Dark Field (HAADF) detection and Electron Disperse X-Ray (EDX) analysis (Brucker X-flash 6 T-30).

The optical properties were evaluated by the Diffuse Reflectance Spectroscopy (DRS) and photoluminescence (PL) techniques. For the DRS-UV–visible analysis, a Varian Cary 5E spectrophotometer was used. The absorbance and reflectance spectra were monitored at 200–2000 nm. From the reflectance signal, the Kubelka-Munk Function, F(R∞) was calculated, and the bandgap was estimated by the Tauc plot method, applying indirect electron transitions. The PL spectra were monitored in a Varian Cary Eclipse fluorimeter, setting an excitation wavelength of 365 nm.

2.3. Photocatalytic production of aldehydes

The photocatalytic behavior of the prepared samples was assessed in the selective oxidation of cinnamyl alcohol (CA) to cinnamaldehyde (CD). However, other selected alcohols such as benzyl alcohol (BA) and vanillin alcohol (VA) were also oxidized to their respective aldehydes (BD, benzaldehyde; VD, vanillin). The photocatalytic experiments were conducted in a jacketed cylindrical photoreactor, in whose center two UVA lamps (365 nm, 9 W each) were placed. The reacting slurry solution (catalyst dose, 0.5 g L^{-1}) was pumped through the annular space. The temperature was controlled at 20 °C with the help of an auxiliary tank containing the alcohol solution (1 mM), which was pumped into the annular space of the photoreactor. Specific details of the setup's scheme and dimensions can be checked in previous works [23,24]. To ensure the presence of dissolved O_2, air was supplied in the auxiliary tank. Before starting the photocatalytic assay, an adsorption period was conducted in the darkness to ensure the adsorption equilibrium. Next, the lamps were switched on, and samples were withdrawn and filtered (Millex PVDF, 0.45 μm) before analysis.

The influence of the oxidative species was evaluated by adding chemical scavengers that suppress certain reactive routes during the oxidation of the alcohol to the aldehyde [25,26]. The role played by the superoxide radical was tentatively analyzed by exchanging air with N_2 bubbling, or the presence of specific inhibitors such as p-benzoquinone (1 mM) or disodium 4,5-dihydroxybenzene-1,3-disulfonate (tiron, 1 mM). The addition of tert-butyl alcohol (TBA, 10 mM) was considered to remove the action of the hydroxyl radicals. Additionally, the formation of hydroxyl radicals was detected by an indirect probe method based on the presence of 2-hydroxy-terephthalic acid (2-HO-TPA) [27,28]. The non-fluorescent terephthalic acid (TPA) displays a strong ability to trap $HO^{\bullet}$, leading to the formation of the fluorescent 2-HO-TPA. A test in the presence of TPA (1 mM) was carried out to potentially probe or discharge the formation of $HO^{\bullet}$. The presence of 2-HO-TPA was analyzed in a Varian Cary fluorescence spectrometer. The excitation wavelength for 2-HO-TPA analysis was set at 315 nm and the emission spectra were recorded at 360–600 nm, defining a maximum peak at roughly 420 nm. The 2-HO-TPA concentration was determined from the peak area with standard solutions in the range 0.5–5 μM. From the calibration curve, a value of 0.21 μM was calculated for the limit of detection. Finally, the action of the photo-generated holes was scavenged with oxalic acid (1 mM) or ethylenediaminetetraacetic acid (EDTA, 1 mM).

High-Pressure Liquid Chromatography (HPLC) technique was used for quantifying the concentration of the alcohols and the aldehydes. The HPLC device was an Alliance 2695 HPLC from Waters™, with a 2998 photodiode array detector. A Zorbas Bonus-RP column (5 μm, 4.6 × 150 mm) was used. The pumped mobile phase (1 mL min^{-1}) was a mixture of 40 % (*v*/v) acetonitrile and 60 % (v/v) ultrapure water acidified with 0.1 % (v/v) of trifluoroacetic acid. The wavelength selected for quantification was 240 nm for CA, 331 nm for CD, 215 nm for BA, 248 nm for BD, 280 nm for VA, and 248 nm for VD.

The temporal reduction of the alcohol concentration was adjusted to a pseudo-first order kinetics. Hence, the calculated pseudo-first order rate constant (k) was compared among the photocatalytic tests. The selectivity of the aldehyde's formation was calculated from the aldehyde and alcohol temporal profiles, and an average value (S) was estimated for comparison purposes.

3. Results

3.1. Characterization of the S-modified g-C_3N_4 samples

The thermal behavior of the three selected precursors during their polymerization was evaluated with thermogravimetric analysis under an N_2 atmosphere. The TGA profiles are depicted in Fig. 2. The pyrolysis of melamine depicts a large mass loss between 300 and 400 °C. Firstly, a rapid deamination of melamine takes place and condensates into melem (2,5,8-triamino-tri-*s*-triazine) and other polymeric derivatives [29]. Over 500 °C, melem is transformed into g-C_3N_4 accompanied by a gradual weight loss as depicted in the TGA of melamine. The TGA profile obtained in the case of thiourea can be divided into three stages. It has been stated that thiourea isomerizes to NH_4SCN in the range 140–180 °C [30], being the proportion thiourea: NH_4SCN roughly 1:3 [31]. Next, the first largest mass loss takes place (76–78 %). In this step the mix of thiourea and NH_4SCN undergoes pyrolysis reactions, leaving the formation of guanidinium thiocyanate and the release of H_2S and NH_2CN [31]. Next, the guanidinium thiocyanate decomposes into melamine and melem at 260–300 °C releasing NH_3 and CS_2 [32]. Finally, from 350 to 450 °C, the decomposition of g-C_3N_4 is deduced [33]. The TGA plot shows three steps for the case of urea. The first loss, appreciated at 160–250 °C, is attributed to vaporization and decomposition into ammonia, cyanic acid, and CO_2 [34]. These gases then react with urea to produce biuret [35]. The second major loss, starting at 230–360 °C, is linked to the degradation of biuret to produce cyanuric acid and ammelide [36], one of the precursors of the tri-s-heptazine aromatic rings of g-C_3N_4. The final mass loss takes place gradually between 360 and 450 °C. In this stage, residual cyanuric acid and ammelide continue their decomposition to produce ammeline, which triggers melamine formation. The formation of stable tri-*s*-triazine rings and their polymerization takes place at over 390 °C, leading to the formation of the g-C_3N_4 [37]. The final structure of g-C_3N_4 is determined mainly by the

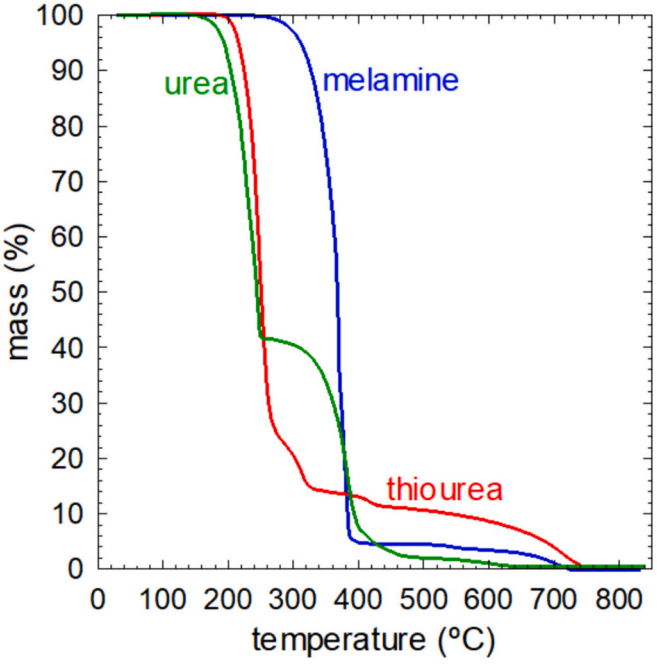

Fig. 2. Thermogravimetric analysis of the g-C_3N_4 precursors under N_2 atmosphere.

reaction produced above 350 °C. The heating rate has been stated as crucial for developing porous structures. Thus, a high heating rate (15 °C min^{-1}) has been demonstrated to scaffold a porous structure, with a high surface area, a complete g-C_3N_4 skeleton, and more amino groups [37], as is the case of the TGA curves of Fig. 2 (heating rate, 20 °C min^{-1}). Temperatures higher than 700 °C promote the complete degradation of the polymeric material. Based on the results achieved by the TGA analysis of the three precursors, it can be concluded that the formation of the g-C_3N_4 occurs by the rearrangement of melamine into melon units, even when using precursors such as thiourea and urea. Temperatures over 500 °C provide optimal conditions for defining the g-C_3N_4 structure, albeit inferior to 700 °C. For this reason, a standard value of 550 °C was set as the temperature for synthesizing the CNx samples. Also, from the results achieved in the TGA, it is appreciated that the production yield was CNt > CNm > CNu.

The XRD technique was conducted to assess the crystallinity of the prepared g-C_3N_4 with the three g-C_3N_4 precursors and their following modification with thiosulfate. Fig. 3A illustrates the diffractograms of the CNx before and after modification with 5 % $Na_2S_2O_3$. The samples displayed the typical feather of g-C_3N_4 with two peaks attributed to the graphite structure and the tri-*s*-triazine units [38]. The most intense peak at approx. 27.4° appears from the piling aromatic units, being the result of the (002) crystal face, interplanar distance of the conjugated units of roughly 0.325 nm. The second peak, much less intense, is the result of the ordered tri-*s*-triazine units in the sheets. This peak was categorized as the (001) diffraction plane, attributed to the intraplanar distance. In this case, the precursor nature influenced the location of this peak, and therefore the d-value, being in the case of CNm 0.68 nm (13.1°), CNt 0.66 nm (13.4°), and CNu 0.68 nm (13.0°). This distance was, in all the cases, smaller than the expected in the tri-*s*-triazine unit, reported as 0.73 nm [39]. This variation can be explained based on a small curvature in the planar structure. The modification with Na_2SO_3 contributed to the decrease of the crystalline peaks, especially the (002) stacking layer. The most intense peak, i.e. (002), was selected for the crystal size calculation, and the number of layers was calculated [22], see Table 1. The results suggest that the $Na_2S_2O_3$ modification led to a decrease in the crystal size, except for the CNt. The sample CNt led to the lowest number of layers, i.e. 19. The CN prepared with melamine described roughly 29 layers and urea led to 24. After treatment with $Na_2S_2O_3$, there was a stable decrease with the concentration defined as 19 layers in the case of CNu. Additionally, peaks at low intensity were registered. Although an attempt to identify the nature of these peaks was conducted, no clear components were found. These peaks are hypothesized to appear as the consequence of Na presence in the structure, as corroborated by XPS. However, the complexity of their interaction with the polymeric structure did not provide any match to the known registered inorganic compounds in the XRD database even in the sample with the best definition of these peaks, i.e. SCNu-10 %. This lack of

Table 1
Crystal (XRD), textural (N_2 isotherms), and optical (DRS-UV–visible) properties of the CNx and SCNx-y% samples.

Sample	$L_{crystal}$ (nm)	n layers	S_{BET} ($m^2\ g^{-1}$)	V_T ($cm^3\ g^{-1}$)	E_{BG} (eV)
CNm	8.5	29	12.5	0.061	2.60
SCNm-5 %	7.8	24	12.8	0.061	2.60
CNt	6.3	19	18.9	0.097	2.64
SCNt-5 %	6.3	19	16.7	0.079	2.66
CNu	7.7	24	69.5	0.318	2.85
SCNu-1 %	7.6	23	69.5	0.288	2.85
SCNu-3 %	7.0	22	66.9	0.284	2.85
SCNu-5 %	6.8	21	64.4	0.214	2.75
SCNu-10 %	6.2	19	40.0	0.177	2.80

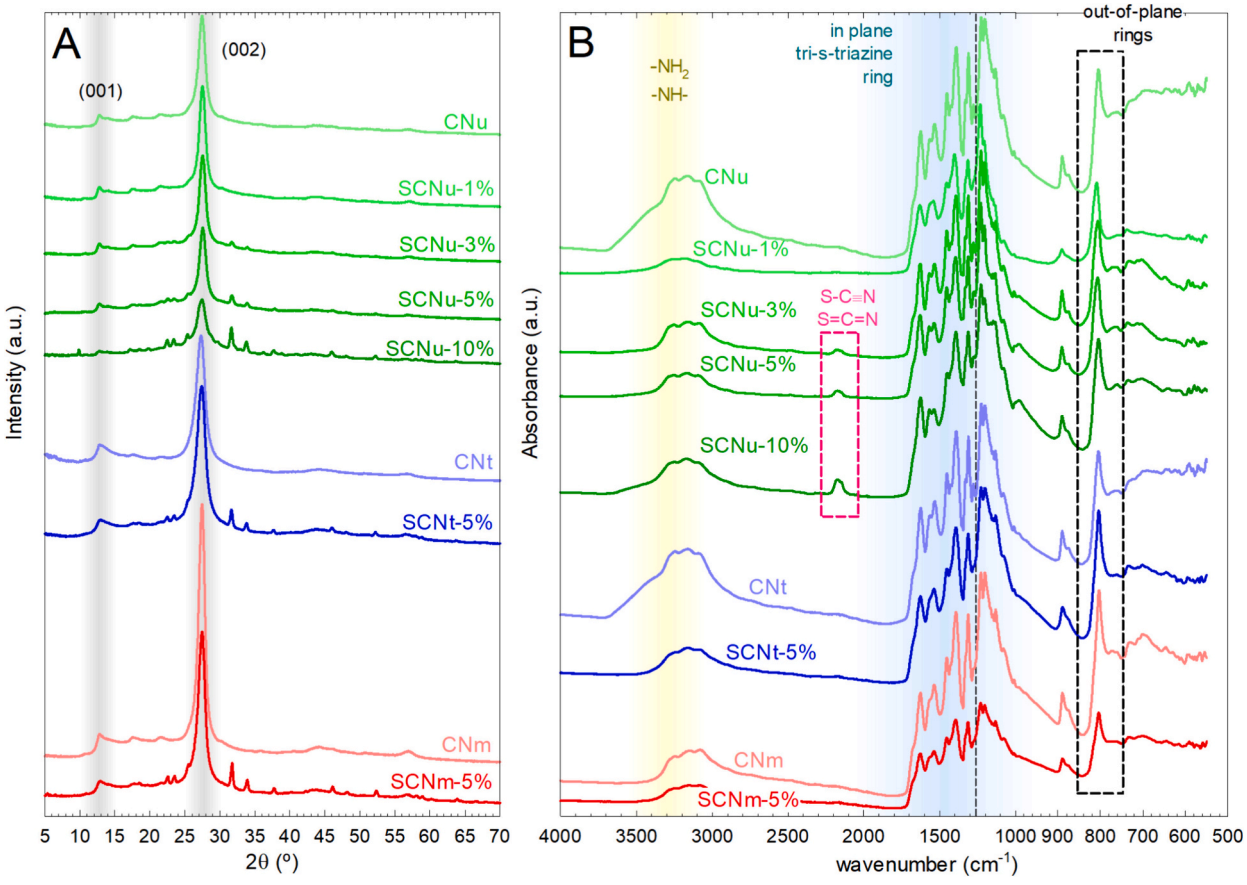

Fig. 3. XRD diffractograms (A) and FTIR spectra (B) of the CNx and SCNx-y% samples.

coincidence evidences the complexity of the interaction of the impurities with the structure, discharging any simpler known Na-related inorganic compound. The doping of g-C_3N_4 with Na^+ has been reported to be combined with the in-plane N atoms in an ionic bond [40], which increases the electron density of the planar CN, with potential boosted separation of the charge carriers upon irradiation [40,41]. The available works dealing with Na-modification with NaOH did not report any appearance of impurities as here with the sample SCNu-10 %, probably due to the low concentration of Na if compared to this sample (10 %) [42,43].

The structural properties of the g-C_3N_4 skeleton were evaluated by FTIR analysis. The FTIR fingerprints of the CN materials are depicted in Fig. 3B and the corresponding modified counterparts with $Na_2S_2O_3$. The three CN samples described the typical fingerprint of this graphite-like sp^2-bonded structure [44]. A broad peak placed 3000–3400 cm^{-1}, is mainly attributed to N—H vibration in the terminal -NH_2 and -NH- [45,46]. Remarkably, the presence of terminal nitrile groups was discharged since there was a complete lack of any peak centered on 2360 cm^{-1} [47]. All the samples described an intensive peak located at 800 cm^{-1}, described due to the vibration among the planes [46,48]. The presence of tri-*s*-triazine rings describes a particular fingerprint in the range 900–1800 cm^{-1}. The most important are those located at 1620, 1530, and 1390 cm^{-1}, described by the stretching vibration of the C—N rings [46,49]. The three precursors led to very similar FTIR spectra. CNu and CNt described the highest contribution of the terminal -NH_2/-NH- groups. In contrast, melamine described the highest peak at 800 cm^{-1}, e.g. the out-of-plane interaction, consistent with the highest peak related to the interplanar layers in the XRD diffractogram. The modification with $Na_2S_2O_3$ implied a certain loss in the definition of the peaks, especially impacted on SCNm-5 %. Interestingly, as the dose of $Na_2S_2O_3$ increased in SCNu, concretely over 3 %, a peak centered at 2160 cm^{-1} augmented its intensity. This peak can be attributed to a thiocyanate (S-C ≡ N) or isothiocyanate (S=C=N) stretching, evidence of sulfur incorporation in the structure by replacing N positions [50,51]. This peak was not registered in the SCNm-5 % and SCNt-5 %. The sample prepared from urea denoted sensitivity for a better reaction with $Na_2S_2O_3$ than the others.

Physisorption analysis was conducted to evaluate the textural properties of the samples. Fig. 4 illustrates the N_2 adsorption-desorption isotherms. All the isotherms can be interpreted, according to the IUPAC classification, with Type II, characteristic of nonporous materials with a large contribution of macropores. The knee is not quite sharp, as it appears at low N_2 uptake in all the samples. This means a significant overlapping of the monolayer, promoting the multilayer formation [52]. Furthermore, the hysteresis loop, attributable to Type H3 according to IUPAC's classification, is commonly observed in aggregated plate-like particles, such as the case of graphitic carbon nitride materials, but also if the pore distribution is predominantly made of macropores which are not filled with pore condensate [52]. The precursor influenced the BET area of the resulting carbon nitride, being CNm (12.5 $m^2\ g^{-1}$) < CNt (18.9 $m^2\ g^{-1}$) < CNu (69.5 $m^2\ g^{-1}$). The total pore volume describes a similar trend. The modification with thiosulfate implied a decrease in the area, as shown in Table 1. Generally, carbon nitride prepared displays low surface area [22], unless a physical or chemical modification is carried out to boost the porosity [53,54]. Regarding the nature of the precursor, the presence of heteroatoms, such as oxygen and sulfur like the respective cases of urea and thiourea, favored the formation of noticeable porosity because of the released volatiles, i.e. CO_2 and CS_2, during the thermal rearrangement of melon units into heptazine units. For this reason, thiourea [55] and urea [56] lead to less crystalline and more porous carbon nitrides. The modification with thiosulfate of the CNm and CNt samples barely defined any substantial change in the surface area when modified at a dose of 5 %. However, in the samples prepared with urea, a slight decrease is appreciated at low thiosulfate dosages (1–5 %), until a considerable area decrease was registered at the highest dose (10 %), i.e. 69.5 $m^2\ g^{-1}$ (CNu) versus 40.0 $m^2\ g^{-1}$ (SCNu-5 %). This considerable decrease may be attributed to a smoothing effect after the reaction on the surface and/or an agglomeration effect during the second thermal treatment.

The composition at the bulk was analyzed by elemental analysis and at the surface level by XPS analysis, see results in Table 2. A detailed analysis of the high-resolution spectra of the CNx and SCNx-5 % samples is depicted in Fig. 5. The C_{1s} peak is frequently deconvoluted in sp^2 N=C-N (287.9 eV), sp^3 C-C/C-N (285.2 eV), and sp^2 C-C/C=C (284.4 eV) contributions [57]. These three contributions were described in all the CNx samples, and an extra contribution in 289–290 eV was observed in the CNm and CNt, probably because of carboxyl, lactone, and ester groups [58]. The modification with thiosulfate did not substantially alter the C_{1s} deconvolution pattern, with a slight increase of the sp^2 C-C/C=C by the loss of sp^3 C-C/C-N. Also, the peak centered at 289–290 eV of oxygenated groups (carboxyl, lactone, and ester) disappeared after treatment probably due to the reducing character of $Na_2S_2O_3$. The N_{1s} region was deconvoluted as the result of three contributions related to N–C=N (N_2C, 398.4 eV), C_3—N (N_3C, 399.9 eV), and terminal N–H_x (401.0 eV) bonds [57,59–61]. The three precursors led to CN materials with the N–C=N outstands. In CNm, the terminal N–H_x follows in

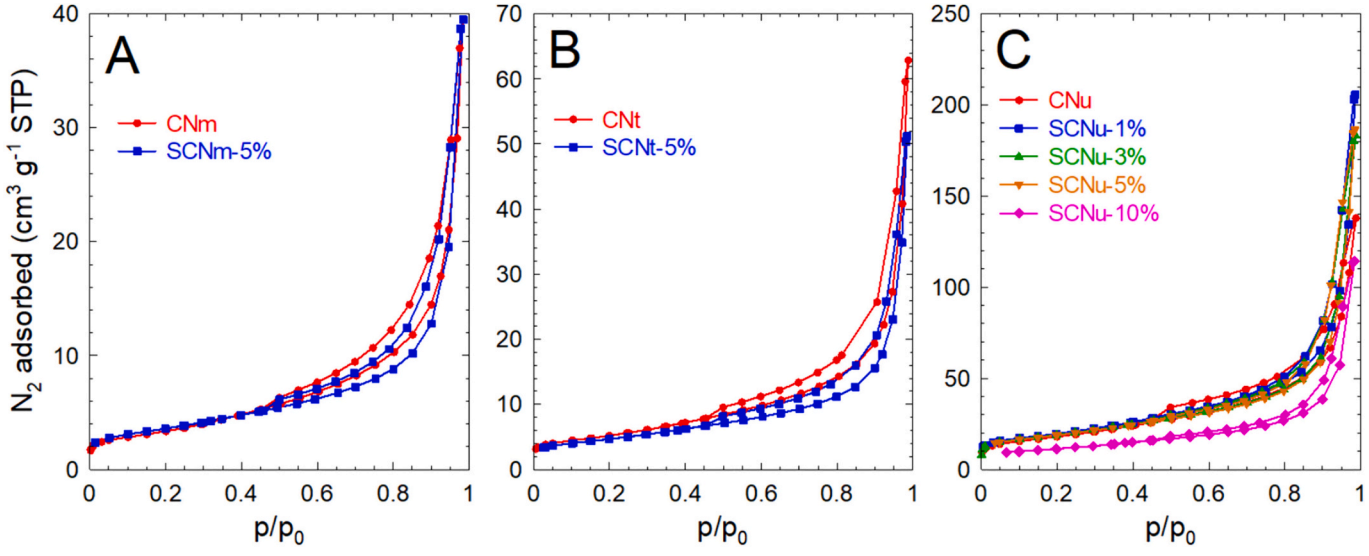

Fig. 4. N_2 adsorption-desorption isotherms at 77 K of the CNx and SCNx-y% samples prepared from melamine (A), thiourea (B), and urea (C).

Table 2
Surface composition by XPS and elemental analysis of the CNx and SCNx-y% samples.

	Elemental analysis (wt%)				XPS (wt%)					VB_{XPS} (eV)
Sample	C	N	H	S	C	N	O	S	Na	
CNm	35.2	63.9	1.9	–	42.5	54.6	2.9	–	–	2.1
SCNm-5 %	32.8	58.9	1.7	2.4	42.7	51.5	4.5	1.0	0.3	2.0
CNt	34.9	62.8	2.0	–	41.0	56.4	2.6	–	–	2.0
SCNt-5 %	34.2	57.6	1.8	2.1	42.9	50.0	5.1	1.3	0.7	2.0
CNu	29.9	53.2	1.8	–	42.8	54.0	3.2	–	–	2.0
SCNu-5 %	31.5	55.5	1.5	2.6	42.3	48.5	5.2	2.4	1.6	2.2

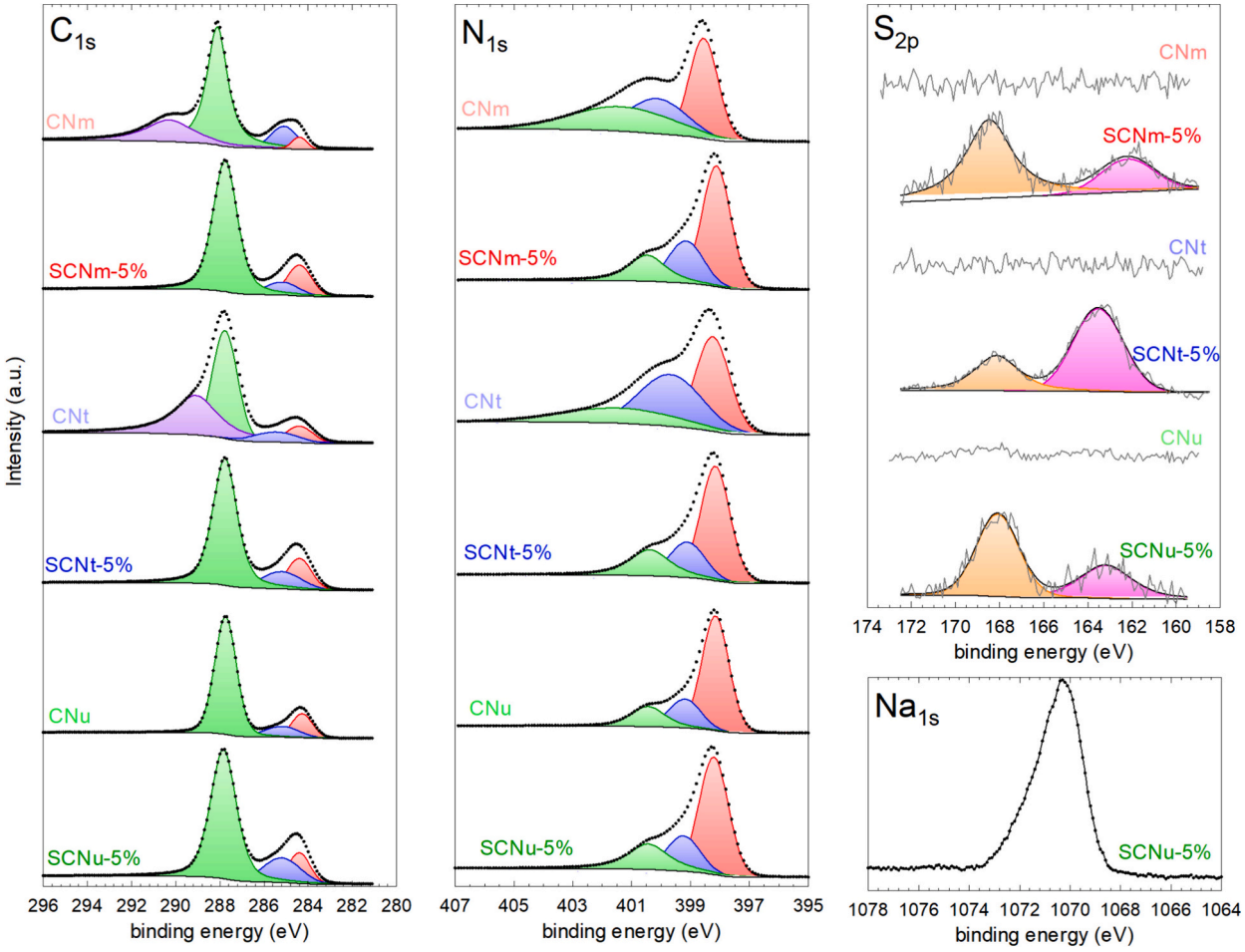

Fig. 5. High-resolution XPS spectra of C_{1s} (left), N_{1s} (middle), S_{2p} (top-right), and Na_{1s} (bottom-right) of the CNx and SCNx-y% samples.

importance to the sp^2 nitrogen, while the CNt the sp^3-N is the second in importance. The sample CNu displayed a good equilibrium between sp^3-N and terminal N–H_x. The modification with thiosulfate assisted in the equilibration of these minor contributions. Regarding the region of S_{2p}, the thiosulfate samples displayed two contributions, one located at 162–164 eV that could be attributed to C-S-C environment [62], and the other placed at 168 eV that can be attributed to C-SO_2- binding [63,64]. The samples SCNm-5 % and SCNu-5 % displayed more contribution of the C-SO_2- than the C-S-C group, while thiourea as precursor had more preference for the C-S-C bonds. According to the surface quantification by XPS, the S content was the highest in the sample SCNu-5 %, e.g. 2.4 %. The thiosulfate modification with the other two precursors led to barely half of the S content. If these results are compared to the elemental analysis, see Table 2, it is appreciated that the three SCNx-5 % samples led to a similar S content of 2.1–2.6 %. The sample SCNu-5 % displayed a uniform distribution of S among all the samples where the SCNm-5 % and SCNt-5 % have the sulfur concentrated in the core rather than on the surface compared to the bulk composition by elemental analysis. The presence of Na^+ cation was confirmed, as depicted in the Na_{1s} spectrum of Fig. 5. A peak centered at 1070.5 eV evidences the presence of Na^+ [43], as reported in previous works focused on incorporating Na^+ and N defects in the graphitic carbon nitride structure [65]. The quantified amount of Na in the SCNx-5 % samples, available in Table 2, varied from 0.3 to 1.6 % depending on the precursor used.

The morphology of CNu and SCNu-5 %, the precursor and thiosulfate-modified with the best photocatalytic active, was examined by the TEM microscopy, leading to the micrographs summarized in Fig. 6. The CNu imaging was characterized by the presence of randomly curved films. These films appeared as wrinkled clusters of over 1 μm, creating cavities as observed in Fig. 6 A_1, supporting the textural mesoporosity deduced from N_2 isotherms. The use of urea is expected to develop a porous material due to the release of CO_2 during its polymerization, providing porous structures composed of pressed sheets with irregular roughness [66–69]. The treatment with thiosulfate led to

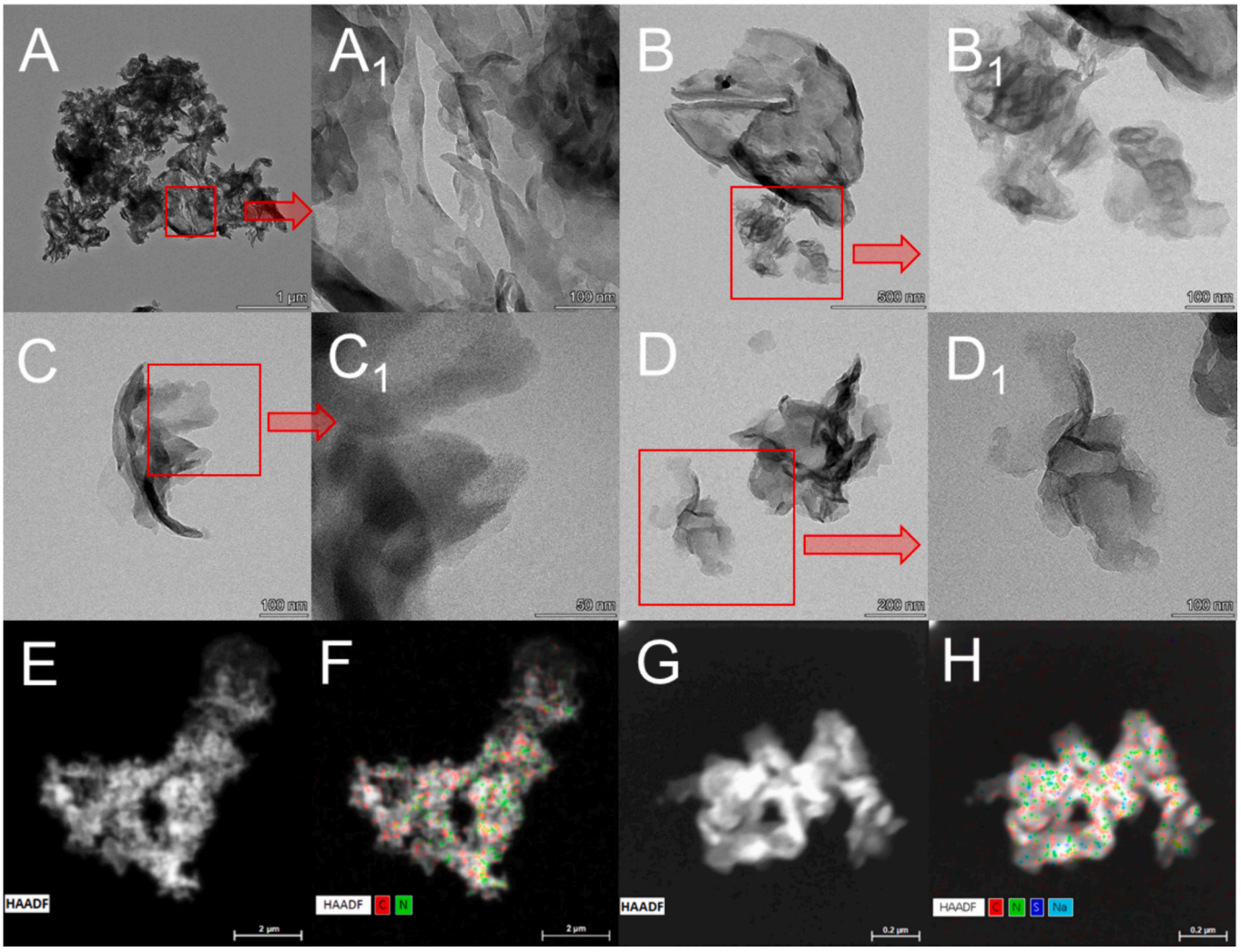

Fig. 6. TEM pictures of CNu (A and B) and SCNu-5 % (C and D). HAADF and element mapping of CNu (E and F) and SCNu-5 % (G and H).

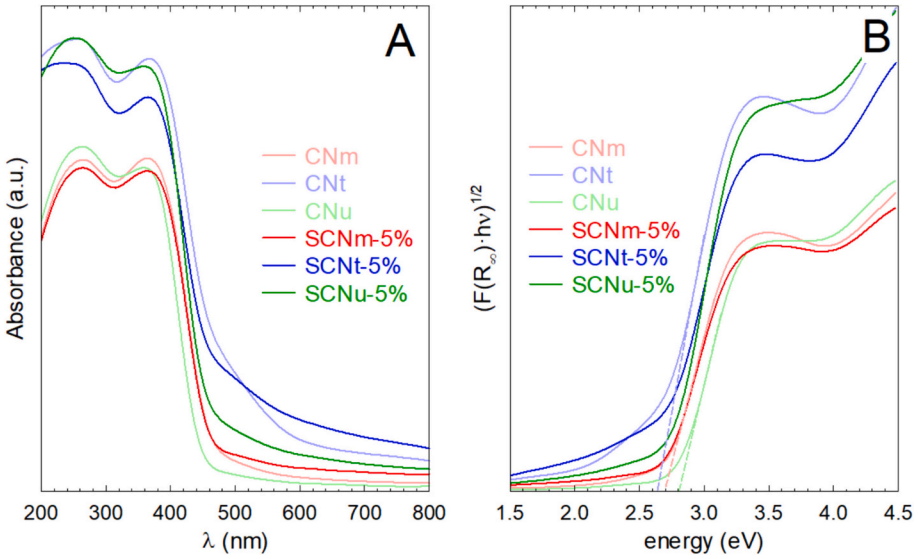

Fig. 7. DRS-UV–visible spectra (A) and Tauc's plot (B) of the CNx and SCNx-5 % samples.

particles of smaller size, up to roughly 500 nm in which the roughness is considerably softened. The presence of sulfur and sodium in the SCNu-5 % was confirmed by EDS mapping although the intensity at which detected was low, due to the low concentration as the quantification by XPS suggested.

The DRS-UV–visible characterization was conducted to evaluate the optical properties. The absorption spectra are portrayed in Fig. 7A, and the bandgap calculation (Table 1) is depicted in Fig. 7B. All the CN photocatalysts performed a strong absorption ability in the visible range, the result of the π-π* electronic transition of the conjugated planes. The lowest absorption of CNu may be the result of the presence of less condensed melem or melon oligomers, a fact corroborated by the lower crystalline structure in this case [70]. This effect impacted the bandgap of the three precursors, i.e. CNm (2.60 eV) ~ CNt (2.66 eV) < CNu (2.85 eV). Poor crystallinity of g-C_3N_4 has been reported to promote an enlargement of the π-π* piling distance, which embraces a wider bandgap and more charge recombination [71], both detrimental for a photocatalytic application. The modification of thiosulfate enlarged the harvesting of radiation in the visible range; therefore, decreasing the bandgap values, which was more appreciable in the case of the largest bandgap CN, i.e. CNu.

3.2. Photocatalytic production of aldehydes

The photocatalytic production of aldehydes with the different graphitic carbon nitride prepared from the different precursors' formulas was first evaluated with the oxidation of cinnamyl alcohol (CA) to cinnamaldehyde (CD). Fig. 8 depicts the time course of the CA concentration and the related pseudo-first order rate constant (k_{CA}). As illustrated, CA was not photolyzed under the source of irradiation used, i.e. UVA of 365 nm. The different precursors lead to g-C_3N_4 with different efficiency in the oxidation of CA. The melamine was the least active g-C_3N_4, $k_{CA} = 0.086\ h^{-1}$. The CNt and CNu improved the results achieved with melamine, leading to similar activity, $k_{CA} = 0.241 \pm 0.019\ h^{-1}$ for CNt and $k_{CA} = 0.265 \pm 0.004\ h^{-1}$ for CNu. The photocatalytic oxidation reactions are triggered on the surface of the semiconductor after irradiation. Both textural and optical properties define the activity of the material. The optical properties of CNm, CNt, and CNu in terms of bandgap or photoluminescence response (see Fig. 8C) cannot solely explain why CNu is the most photoactive. In this case, it seems that the surface area, much higher in the CNu sample, is the key factor.

The modification with thiosulfate of the CNx samples led to different behavior depending on the precursor. Regarding melamine, the photocatalytic activity of CNm-5 % was improved concerning the bare CNm, although the increase in the k_{CA} was limited, from 0.086 ± 0.003 to 0.224 ± 0.005 h^{-1}. In the case of thiourea, the modification with thiosulfate led to a detrimental effect, negatively affecting the oxidation kinetics of CA, 0.241 ± 0.019 to 0.136 ± 0.003 h^{-1}. The modification with 5 % of $Na_2S_2O_3$ did not substantially change the surface area of the CNx samples. Therefore, the differences in photocatalytic activity may rely on the optical properties. According to the photoluminescence of the samples, see Fig. 8C, the PL peak of thiourea was increased after the thiosulfate treatment, leading to a poorer separation of charges. The analysis by photoluminescence has been linked to the electronic behavior of a semiconductor after irradiation. Hence, after excitation, the electron-hole pair recombination leads to the emission of a photon of energy equal to the bandgap energy. Therefore, a low-intensity PL peak can be associated with a lower recombination effect, undesirable phenomenum for efficient radiation harvesting [72]. The incorporation of sulfur and Na^+ contributed to imperfections that minimized the electronic recombination after excitation [40,42,43], leading to enhanced photocatalytic activity. The photocatalytic activity described by CNt and SCNt-5 % is under the response registered by PL. The CNu modification, i.e. SCNu-5 %, led to the best improvement compared to the rest of the used precursors. In this case, the k_{CA} was remarkably augmented from 0.265 ± 0.004 to 0.792 ± 0.044 h^{-1}, which means 3 times folded. The PL intensity of the SCNu-5 % was considerably lower than the counterpart CNu; therefore, the modification with thiosulfate improved the charge separation rate, minimizing the recombination effect that positively impacts the activity performance. As the modification of CNu led to the best result, the proportion of thiourea was assessed for this sample.

Fig. 9 depicts the effect of the thiosulfate ratio during the modification of CNu. As illustrated, it is observed that the proportion of thiosulfate reaches an optimum value for the kinetics of CA oxidation, located at 5 %. The k_{CA} values matched the behavior of the PL peak, being the activity inverse to the intensity of the emission peak, CNu-5 % (0.792 ± 0.044 h^{-1}) > CNu-10 % (0.682 ± 0.044 h^{-1}) > CNu-3 % (0.615 ± 0.040 h^{-1}) > CNu-1 % (0.341 ± 0.012 h^{-1}) > CNu (0.265 ± 0.004 h^{-1}). Therefore, the modification with thiosulfate could be ascribed to the minimization of the recombination effect by the definition of imperfections on the surface, despite the case of SCNu-10 % in which a decrease of the surface area, and therefore the active reacting sites, was observed.

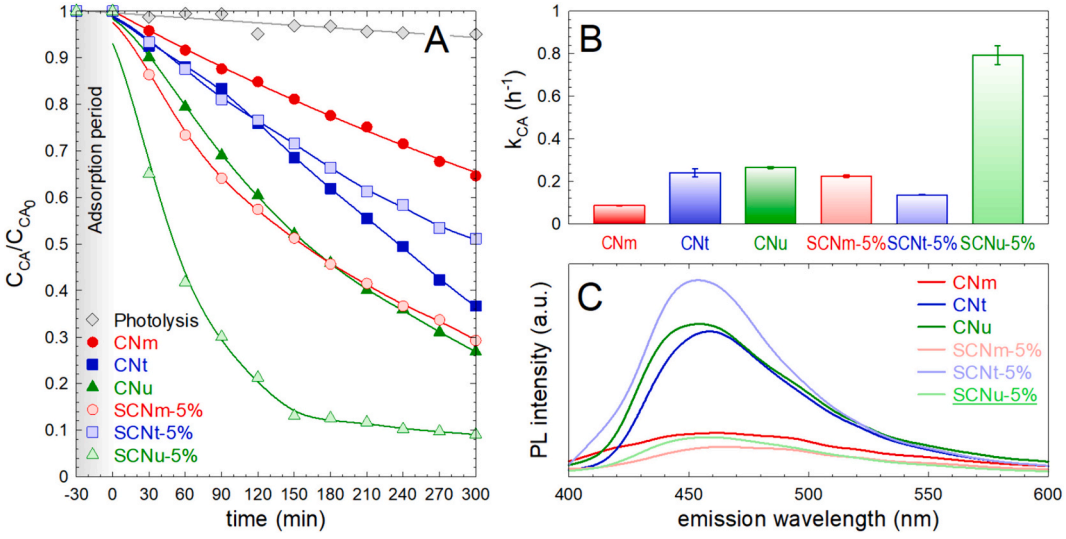

Fig. 8. Photocatalytic oxidation of cinnamyl alcohol with CNx and SCNx-5 % samples. (A) Time-course of the CA normalized concentration. (B) Pseudo-first order rate constant of CA abatement. (C) Photoluminescence spectra of CNx and SCNx-5 % samples. Experimental conditions: UVA radiation; V = 350 mL; C_{CA} = 1 mM; $C_{catalyst} = 0.5\ g^{-1}$, T = 20 °C.

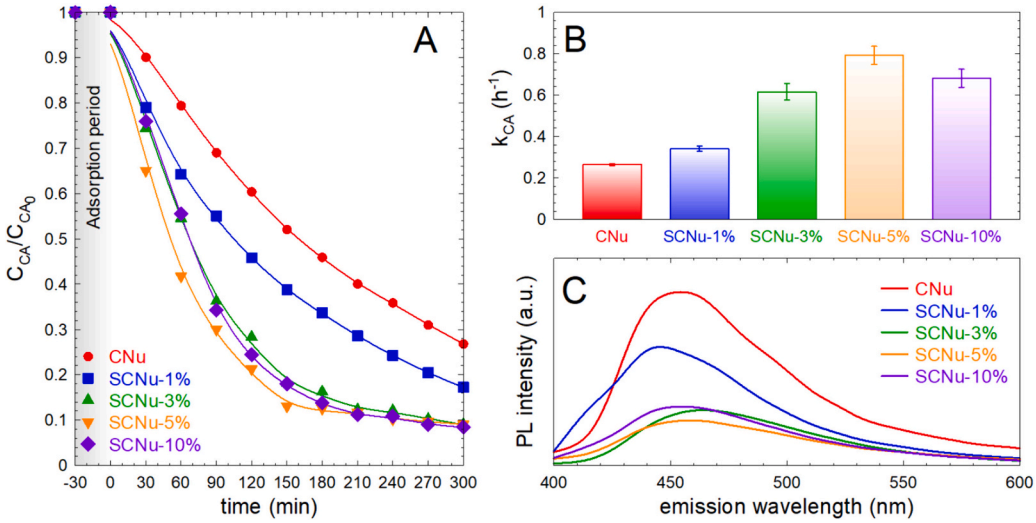

Fig. 9. Photocatalytic oxidation of cinnamyl alcohol with SCNu-y% samples. (A) Time-course of the CA normalized concentration. (B) Pseudo-first order rate constant of CA abatement. (C) Photoluminescence spectra of SCNu-y% samples. Experimental conditions: UVA radiation; V = 350 mL; $C_{CA} = 1$ mM; $C_{catalyst} = 0.5\,g^{-1}$, T = 20 °C.

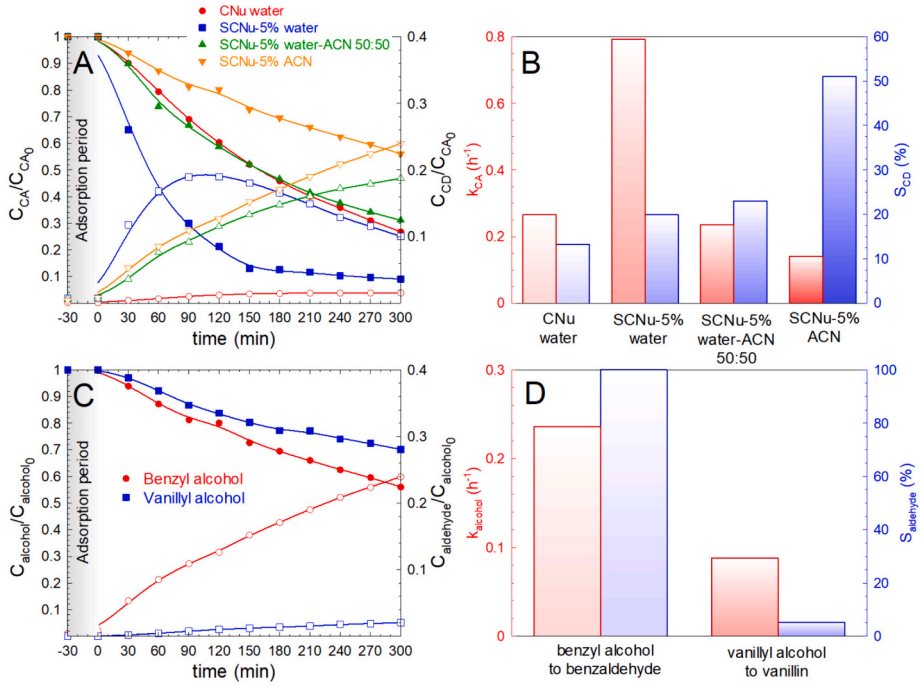

Fig. 10. Time-course of CA and CD (empty symbols) concentration during the photocatalytic oxidation with SCNu-5 % in water, acetonitrile (ACN), and 50:50 mixtures (A). Pseudo-first order rate constant of CA oxidation and average selectivity to CD (B). Temporal evolution of benzyl alcohol, vanillyl alcohol, and their respective aldehydes (empty symbols) during the photocatalytic oxidation with SCNu-5 % in water (C). Pseudo-first order rate constant of benzyl and vanillyl alcohol oxidation and their average selectivity to their respective aldehydes (D). Experimental conditions: UVA radiation; V = 350 mL; $C_{alcohol} = 1$ mM; $C_{catalyst} = 0.5\,g^{-1}$, T = 20 °C.

Based on the greater photocatalytic performance during CA oxidation, the sample SCNu-5 % was selected for further study. Fig. 10 portrays the average selectivity during the 5 h of CA oxidation to CD. The selectivity of the SCNu-5 % sample was ~20 % whereas the non-modified CNu achieved 13 %. More interestingly, not only did the nature of the solvent impact kinetics but also the selectivity. In the presence of acetonitrile (ACN), the sample SCNu-5 % led to a reduction of the k_{CA} to $0.140 \pm 0.007\ h^{-1}$. However, selectivity was boosted to 51 % in the presence of ACN. The use of a water-ACN mixture at 50:50 described intermediate k_{CA} and selectivity values. In the presence of water, cinnamyl alcohol displays great reactivity. The aldehyde formation passes through a hydration step to form a geminal diol in the presence of water, which then dehydrogenates to trigger the corresponding acid, making the transient aldehyde formed undetected in the reaction medium [1]. In the specific case of cinnamaldehyde, the hydration and further oxidation to form cinnamic acid have been reported as important [1]. This fact explains why the selectivity of CA decays in the presence of water if compared to organic solvents such as acetonitrile or toluene [73]. Moreover, the presence of organic solvent also promotes a higher solubility of O_2 if compared to water [74]. The lack of

water and the higher dissolved O_2 may lead to a better generation of superoxide radicals and photogenerated holes, positively impacting the selectivity to the aldehyde [23].

The effectiveness of the SCNu-5 % sample in water was also tested in the oxidation of other aromatic alcohols, such as benzyl and vanillyl alcohol, generating their respective aldehydes. Fig. 10C depicts the time course of each alcohol and its aldehyde. In the case of benzyl alcohol (BA), it is observed that the reactivity is lower than the observed for cinnamyl alcohol, $k_{CA} = 0.792 \pm 0.044$ vs $k_{BA} = 0.236 \pm 0.007$ h^{-1}. Nonetheless, the oxidation was exclusively oriented to the production of benzaldehyde, leading to a selectivity of 100 %. In the case of the oxidation of vanillyl alcohol (VA), it was not the case. This alcohol was the least reactive to the SCNu-5 % sample, $k_{VA} = 0.088 \pm 0.003$ h^{-1}, with a poor selectivity to vanillin (VD), only 5 %.

The impact of the different Reactive Oxidative Species (ROS) involved in the oxidation of cinnamyl alcohol has been elucidated by adding to the reaction medium different chemical scavengers that inhibit certain species associated with a higher affinity towards them [75–77]. Fig. 11A shows the temporal evolution of CA concentration in the presence of inhibitors. The influence of superoxide radical ($O_2^{\bullet-}$), generated after adsorbed O_2 is reduced by the photogenerated electrons of the conduction band was evaluated by exchanging the air bubbling with N_2, with the addition of chemical scavengers such as p-benzoquinone (p-BZQ) or tiron [23,78]. In the presence of N_2, the k_{CA} was reduced, as illustrated in Fig. 11B, which proves the importance of $O_2^{\bullet-}$ in the overall oxidative mechanism. However, the absence of O_2 may contribute to a higher recombination effect since the photogenerated electrons are not consumed. A test with p-BZQ was conducted. The kinetics was considerably decelerated, i.e. k_{CA} was 30 % of the blank test. Although this fact would mean considerable participation of $O_2^{\bullet-}$, the results must be interpreted with caution due to the complex chemistry of p-BZQ which may lead to alternative side-chain reactions [76], such as reaction with $HO^{\bullet}$, formation of semiquinone radicals [25], or photolysis that produces extra $O_2^{\bullet-}$ [79] or $^1O_2$ [80]. For this reason, tiron was also assessed as an alternative scavenger [76]. In the presence of tiron, the k_{CA} value was not substantially altered as observed with p-BZQ.

The role played by the $HO^{\bullet}$ was evaluated in the presence of tert-butyl alcohol (TBA), due to its high affinity [81]. In the test with TBA, the CA oxidation kinetic was barely altered; therefore, the influence of $HO^{\bullet}$ must be discharged. To further confirm the lack of $HO^{\bullet}$, a probe test of 2-hydroxy-terephthalic acid (2-HO-TPA) from the reaction of terephthalic acid (TPA) with $HO^{\bullet}$ was conducted [27]. According to the considerable signal-to-noise ratio of the fluorescent spectra registered for 2-HO-TPA with the temporal evolution (Fig. 11C), the amount of 2-HO-TPA could be predicted as negligible. The quantification led to the temporal profile of 2-HO-TPA depicted in Fig. 11D, whose values were all below the limit of detection of the method, stimated as 0.21 μM, a value much lower than the detected in photocatalytic processes with a predominant role of the $HO^{\bullet}$ route [28,82].

The plausible contribution of the photogenerated holes to the oxidative mechanism was assessed by two traditional hole-scavengers, the oxalate anion [83] and ethylenediaminetetraacetic acid (EDTA) [83,84]. The addition of oxalate anion decelerated the kinetics of CA oxidation while EDTA kept it like the blank test. Interestingly, selectivity was raised in both cases, which may be proof of a more selective oxidation process in the absence of the photogenerated holes. It should be considered that the presence of these substances positively contributes to the kinetics of the process in some cases since it favors the insertion of extra photogenerated electrons to the conduction band as the holes are consumed. The faster and greater removal in the presence of EDTA compared to oxalate has been confirmed as superior due to the hole consumption by EDTA [83]. Therefore, it seems that the presence of holes contributes to the degradation process, negatively affecting the selectivity of the process if compared to the superoxide radical. Finally, the contribution of single oxygen was evaluated by adding L-histidine (L-H) to the aqueous medium [26]. Nonetheless, the addition of L-H did not modify the kinetics of the process.

A plausible mechanism of photo-activation with the band alignment

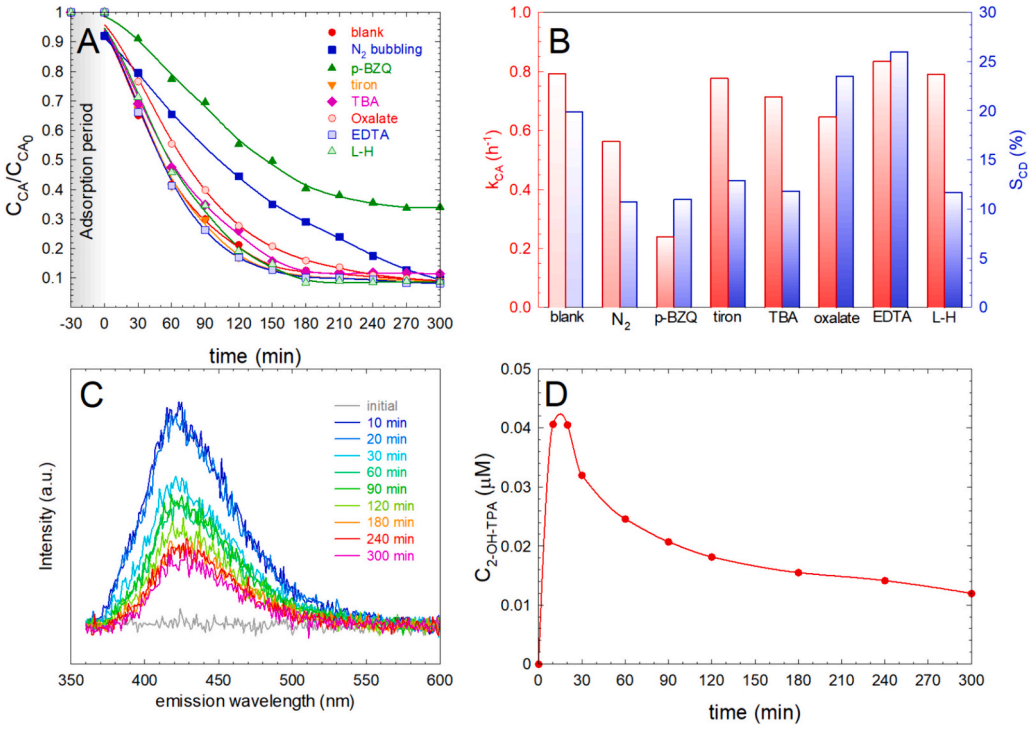

Fig. 11. Photocatalytic oxidation of cinnamyl alcohol (CA) to cinnamaldehyde (CD). The pseudo-first order rate constant of CA abatement with SCNu-5 % in the presence of chemical scavengers (A), the CA conversion at 5 h and average selectivity to CD (B). Photoluminescence spectra of 2-OH-TPA (C) and the temporal evolution of the concentration of 2-OH-TPA (D) during the photocatalytic transformation of TPA with SCNu-5 %. Experimental conditions: UVA radiation; V = 350 mL; $C_{CA,0} = 1$ mM; $C_{SCNu\text{-}5\%} = 0.5$ g L^{-1}; $C_{scavenger} = 1$ mM; $C_{TPA,0} = 1$ mM; T = 20 °C.

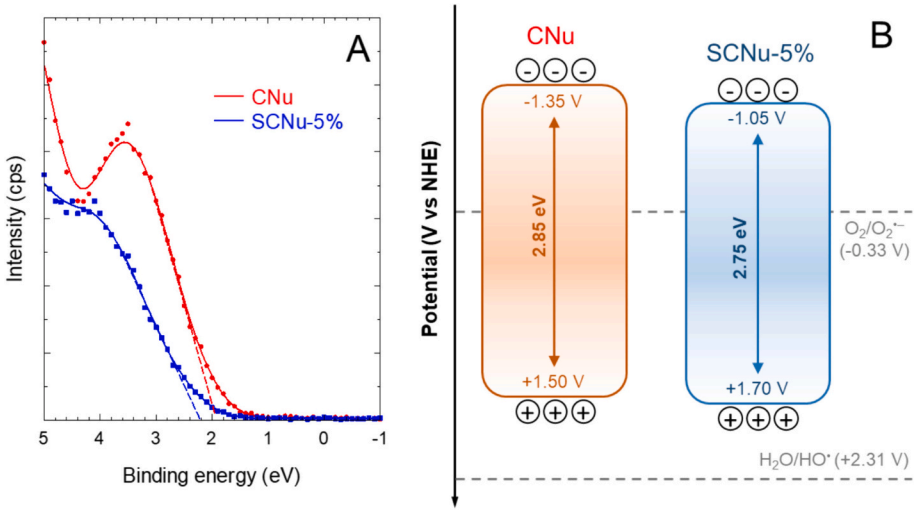

Fig. 12. Estimation of the valence band edge of CNu and SCNu-5 % by XPS (A) and their band's alignment proposal (B).

for CNu and SCN-5 % is proposed in Fig. 12. The valence band energy level was tentatively estimated from the energy edge of XPS (VB_{XPS}) at low energy values, see Fig. 12A. The Fermi level is above the estimated VB_{XPS} value [85,86]. Furthermore, the band edge positions of the valence band (E_{VB}) can be calculated as follows [87,88]:

$$E_{VB} = \Delta E - E_{vac} + W_S \quad (1)$$

where ΔE stands for the difference between the E_F level and the VB maximum value, E_{vac} is the energy of free electrons in the hydrogen scale (4.5 eV), and W_S means the work function. The work function W_S can be considered 4.0 eV for g-C_3N_4 materials [89]. Table 2 shows all the XPS edge values for the CNx and SCNx-5 % samples. All the CNx materials display very similar energy edges in their XPS spectra, around +2.0 eV, i.e. their E_{VB} is +1.5 eV. However, concerning the values of the SCNx-5 %, it was only the sample prepared with urea the precursor that performed an enlargement of the value, concretely the XPS valence band was +2.2 eV, i.e. the E_{VB} = +1.70 eV. This shifted value after thiosulfate modification implies a higher oxidative potential of the holes of the modified photocatalyst. From the estimated E_{VB}, the conduction band energy (E_{CB}) was determined by subtracting the bandgap energy from the E_{VB}, leading to E_{CB} = −1.35 eV for CNu and E_{CB} = −1.05 eV for SCNu-5 %. The value obtained in this work for CNu is within the range of values reported in the literature [90]. A scheme of the band's alignment is portrayed in Fig. 12B for CNu and SCNu-5 %. According to this band placement, it is stated the unfeasibility of the formation of $HO^{\bullet}$, since the redox of the pair $H_2O/HO^{\bullet}$ is +2.31 V [91]. Conversely, the production of the $O_2^{\bullet-}$ is favored, with redox potential $O_2/O_2^{\bullet-}$, −0.33 V [92]. The contrast of the band's energy before and after modification with thiosulfate led to an increase in the redox potential of the photogenerated holes. This fact and the enhanced migration of charges from the photoluminescence emission spectra can be attributed as the main reasons for the boosted photocatalytic activity difference after thiosulfate modification.

The sample with the optimum activity, i.e. SCNu-5 %, was submitted to sequential recycling and reusing tests to examine the material's stability. Fig. 13A depicts the cinnamyl alcohol evolution during four consecutive experiments in water and Fig. 13B illustrates the pseudo-first order rate constant calculated from each one. As depicted, no significant loss of activity was observed. The time-course curves were completely overlapped among them, with an insignificant deviation at the beginning of the assay. The alcohol conversion over 180 min was the same in all the runs. Besides, the pseudo-first order rate constant was kept stable with a minimal decrease, i.e. 0.792 h^{-1} (1st run), 0.763 h^{-1} (2nd run), 0.693 h^{-1} (3rd run), and 0.677 h^{-1} (4th run), which evidences

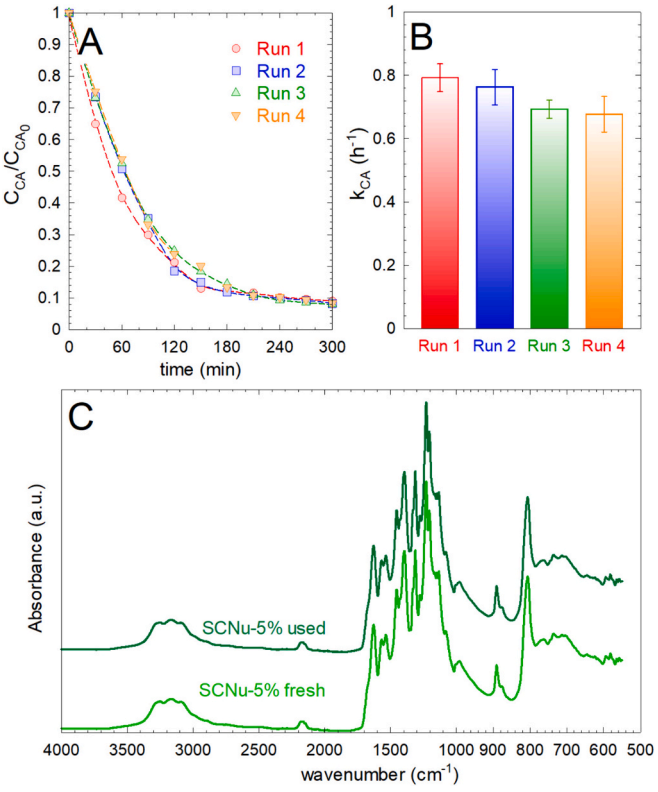

Fig. 13. Stability tests of SCNu-5 % sample. (A) Time-course of the CA normalized concentration. (B) Pseudo-first order rate constant of CA abatement. (C) FTIR spectra before and after use. Experimental conditions: UVA radiation; V = 350 mL; C_{CA} = 1 mM; $C_{catalyst}$ = 0.5 g^{-1}, T = 20 °C.

the great stability of the material. The material recovered from the last run was characterized by FTIR. As shown in Fig. 13C, the characteristic absorbance footprint of the material was maintained, discharging structural changes after its use.

4. Conclusions

Photocatalytic reactions provide a new platform for synthesizing added-value organic compounds such as aldehydes from the oxidation of their alcohols. Hence, the reaction of alcohol oxidation under ambient

temperature and pressure conditions, water as a solvent instead of the traditional expensive and toxic organic solvents, and a metal-free cheaper catalyst such as graphitic carbon nitride has been examined.

The nature of the nitrogen carbonaceous precursor strongly impacts the crystalline and textural properties of graphitic carbon nitride formulas, leading to the use of melamine for a more crystalline and less porous g-C_3N_4, due to the important gases released during the pyrolysis process of thiourea and, especially urea, which leaves imperfections in the structure. In the case of thiourea, and remarkably urea, the synthesized g-C_3N_4 was less crystalline and more porous. This aspect is essential in photocatalytic performance, with the g-C_3N_4 prepared with thiourea and urea being the most active. The oxidation rate constant of cinnamyl alcohol was 0.086 ± 0.003 h^{-1} for the material prepared with melamine, 0.241 ± 0.019 h^{-1} with thiourea, and 0.265 ± 0.004 h^{-1} with urea (initial alcohol concentration, 1 mM). The modification with sodium thiosulfate incorporated enhanced the photocatalytic activity, in the g-C_3N_4 prepared from melamine and urea, being the latter considerable, i.e. the pseudo-first order rate constant of cinnamyl alcohol oxidation k_{CA} = 0.792 ± 0.044 h^{-1}. This improvement was ascribed to the better separation of charges and reduction of the recombination effect as suggested by the photoluminescence characterization, originated by the creation of imperfections on the carbon nitride base, raising the oxygen content and incorporating S as thiocyanate/isothiocyanate, C-S-C, and C-SO_2 bonds. The selectivity to cinnamyl alcohol of the thiosulfate sample prepared with urea was enhanced from 13 % (bare g-C_3N_4) to 23 % in aqueous solution. This value was further boosted by replacing the aqueous media with acetonitrile, increasing it to 51 %. This sample demonstrated higher effectiveness in oxidizing benzyl alcohol to benzaldehyde, i.e. 100 % selectivity. The study of the mechanism of the reacting species involved in the process suggested the importance of superoxide radicals and holes, the former being more selective. The hydroxyl radical impact was negligible due to insufficient energy for the oxidation of water molecules.

CRediT authorship contribution statement

M. Alejandra Quintana: Methodology, Investigation. **Julia Aguirre**: Investigation. **M. Ángeles Martín-Lara**: Investigation, Writing – review & editing. **Mónica Calero**: Resources, Writing – review & editing, Funding acquisition. **Mario J. Muñoz-Batista**: Writing – review & editing, Supervision, Funding acquisition. **Rafael R. Solís**: Conceptualization, Investigation, Formal analysis, Writing – original draft, Visualization, Supervision.

Declaration of competing interest

The authors declare that they have no known competing financial interests or personal relationships that could have appeared to influence the work reported in this paper.

Data availability

Data will be made available on request.

Acknowledgments

This work has received funds from the project PID2022-139014OB-I00/SRA(State Research Agency)/10.13039/501100011033. The authors also thank the help characterizing the solid samples provided by the CIC (*Centro de Instrumentación Científica*) of the University of Granada. Julia Aguirre thanks the Ministry of Education, Vocational Training, and Sports for her Collaboration Scholarship in the Chemical Engineering Department of the University of Granada during the academic year 2023-2024. Funding for open access charge: Universidad de Granada/CBUA.

References

[1] M. Besson, P. Gallezot, Selective oxidation of alcohols and aldehydes on metal catalysts, Catal. Today 57 (2000) 127–141, https://doi.org/10.1016/S0920-5861(99)00315-6.
[2] D. Romano, R. Villa, F. Molinari, Preparative biotransformations: oxidation of alcohols, ChemCatChem 4 (2012) 739–749, https://doi.org/10.1002/CCTC.201200042.
[3] B. Muhoza, B. Qi, J.D. Harindintwali, M.Y.F. Koko, S. Zhang, Y. Li, Encapsulation of cinnamaldehyde: an insight on delivery systems and food applications, Crit. Rev. Food Sci. Nutr. 63 (2023) 2521–2543, https://doi.org/10.1080/10408398.2021.1977236.
[4] J. Guo, S. Yan, X. Jiang, Z. Su, F. Zhang, J. Xie, E. Hao, C. Yao, Advances in pharmacological effects and mechanism of action of cinnamaldehyde, Front. Pharmacol. 15 (2024) 1365949, https://doi.org/10.3389/FPHAR.2024.1365949.
[5] A.A. Doyle, J.C. Stephens, A review of cinnamaldehyde and its derivatives as antibacterial agents, Fitoterapia 139 (2019) 104405, https://doi.org/10.1016/J.FITOTE.2019.104405.
[6] Z. Zhou, Y.N. Xie, W. Zhu, H. Zhao, N. Yang, G. Zhao, Selective photoelectrocatalytic tuning of benzyl alcohol to benzaldehyde for enhanced hydrogen production, Appl. Catal. B 286 (2021) 119868, https://doi.org/10.1016/J.APCATB.2020.119868.
[7] G.A. Martău, L.F. Călinoiu, D.C. Vodnar, Bio-vanillin: towards a sustainable industrial production, Trends Food Sci. Technol. 109 (2021) 579–592, https://doi.org/10.1016/J.TIFS.2021.01.059.
[8] S.K. Upadhyay, S.P. Singh, Plants as Source of Essential Oils and Perfumery Applications, in: Bioprospecting of Plant Biodiversity for Industrial Molecules, John Wiley & Sons Ltd, 2021, pp. 261–292, https://doi.org/10.1002/9781119718017.CH13.
[9] F. Liaqat, L. Xu, M.I. Khazi, S. Ali, M.U. Rahman, D. Zhu, Extraction, purification, and applications of vanillin: a review of recent advances and challenges, Ind. Crop. Prod. 204 (2023) 117372, https://doi.org/10.1016/J.INDCROP.2023.117372.
[10] S.S. Arya, J.E. Rookes, D.M. Cahill, S.K. Lenka, Vanillin: a review on the therapeutic prospects of a popular flavouring molecule, Adv. Tradit. Med. 21 (2021) 1–17, https://doi.org/10.1007/S13596-020-00531-W.
[11] G. Marcì, E.I. García-López, L. Palmisano, Polymeric carbon nitride (C_3N_4) as heterogeneous photocatalyst for selective oxidation of alcohols to aldehydes, Catal. Today 315 (2018) 126–137, https://doi.org/10.1016/J.CATTOD.2018.03.038.
[12] R. Ciriminna, A. Fidalgo, F. Meneguzzo, F. Parrino, L.M. Ilharco, M. Pagliaro, Vanillin: the case for greener production driven by sustainability megatrend, ChemistryOpen 8 (2019) 660–667, https://doi.org/10.1002/OPEN.201900083.
[13] G.K.T. Luong, Y. Ku, Selective oxidation of benzyl alcohol in the aqueous phase by TiO_2-based photocatalysts: a review, Chem. Eng. Technol. 44 (2021) 2178–2190, https://doi.org/10.1002/CEAT.202100321.
[14] F. Su, S.C. Mathew, G. Lipner, X. Fu, M. Antonietti, S. Blechert, X. Wang, Mpg-C_3N_4-catalyzed selective oxidation of alcohols using O_2 and visible light, J. Am. Chem. Soc. 132 (2010) 16299–16301, https://doi.org/10.1021/JA102866P.
[15] G.S. Priyanga, G. Pransu, S. Sampath, A comprehensive overview of the graphitic-carbon nitride computational approach: from basic properties to a wide range of applications, Chem. Phys. Impact 8 (2024) 100408, https://doi.org/10.1016/J.CHPHI.2023.100408.
[16] G. Panthi, M. Park, Graphitic carbon nitride/zinc oxide-based Z-scheme and S-scheme heterojunction photocatalysts for the photodegradation of organic pollutants, Int. J. Mol. Sci. 24 (2023) 15021, https://doi.org/10.3390/IJMS241915021.
[17] S. Kumar, V.R. Battula, K. Kailasam, Single molecular precursors for C_xN_y materials- blending of carbon and nitrogen beyond g-C_3N_4, Carbon N. Y. 183 (2021) 332–354, https://doi.org/10.1016/J.CARBON.2021.07.025.
[18] A. Mohammad, P. Chandra, M.E. Khan, C.H. Choi, T. Yoon, Sulfur-doped graphitic carbon nitride: tailored nanostructures for photocatalytic, sensing, and energy storage applications, Adv. Colloid Interf. Sci. 322 (2023) 103048, https://doi.org/10.1016/J.CIS.2023.103048.
[19] O.M. Bankole, T.D. Olorunsola, A.S. Ogunlaja, Photocatalytic decontamination of toxic hexavalent chromium in water over graphitic carbon nitride supported sulfur nanoparticles, J. Photochem. Photobiol. A Chem. 405 (2021) 112934, https://doi.org/10.1016/J.JPHOTOCHEM.2020.112934.
[20] J. Zhong, T. Ni, J. Huang, D. Li, C. Tan, Y. Liu, P. Chen, C. Wen, H. Liu, Z. Wang, W. Lv, G. Liu, Directional utilization disorder charge via in-plane driving force of functionalized graphite carbon nitride for the robust photocatalytic degradation of fluoroquinolone, Chem. Eng. J. 442 (2022) 135943, https://doi.org/10.1016/J.CEJ.2022.135943.
[21] A. Altomare, N. Corriero, C. Cuocci, A. Falcicchio, A. Moliterni, R. Rizzi, QUALX2.0: a qualitative phase analysis software using the freely available database POW_COD, J. Appl. Crystallogr. 48 (2015) 598–603, https://doi.org/10.1107/S1600576715002319.
[22] Á. Pérez-Molina, L.M. Pastrana-Martínez, S. Morales-Torres, F.J. Maldonado-Hódar, Photodegradation of cytostatic drugs by g-C_3N_4: synthesis, properties and performance fitted by selecting the appropriate precursor, Catal. Today 418 (2023) 114068, https://doi.org/10.1016/J.CATTOD.2023.114068.
[23] M.A. Quintana, A. Picón, M.Á. Martín-Lara, M. Calero, M.J. Muñoz-Batista, R. R. Solís, Towards the photocatalytic production of cinnamaldehyde with phosphorous-tailored graphitic-like carbon nitride, Appl. Catal. A Gen. 674 (2024) 119607, https://doi.org/10.1016/J.APCATA.2024.119607.
[24] R.R. Solís, M.A. Quintana, M.Á. Martín-Lara, A. Pérez, M. Calero, M.J. Muñoz-Batista, Boosted activity of g-C_3N_4/UiO-66-NH_2 heterostructures for the

photocatalytic degradation of contaminants in water, Int. J. Mol. Sci. 23 (2022) 12871, https://doi.org/10.3390/IJMS232112871/S1.
[25] J.T. Schneider, D.S. Firak, R.R. Ribeiro, P. Peralta-Zamora, Use of scavenger agents in heterogeneous photocatalysis: truths, half-truths, and misinterpretations, Phys. Chem. Chem. Phys. 22 (2020) 15723–15733, https://doi.org/10.1039/d0cp02411b.
[26] M. Pelaez, P. Falaras, V. Likodimos, K. O'Shea, A.A. de la Cruz, P.S.M. Dunlop, J. A. Byrne, D.D. Dionysiou, Use of selected scavengers for the determination of NF-TiO_2 reactive oxygen species during the degradation of microcystin-LR under visible light irradiation, J. Mol. Catal. A Chem. 425 (2016) 183–189, https://doi.org/10.1016/j.molcata.2016.09.035.
[27] K.I. Ishibashi, A. Fujishima, T. Watanabe, K. Hashimoto, Detection of active oxidative species in TiO_2 photocatalysis using the fluorescence technique, Electrochem. Commun. 2 (2000) 207–210, https://doi.org/10.1016/S1388-2481(00)00006-0.
[28] A. Gómez-Avilés, R.R. Solís, E.M. García-Frutos, J. Bedia, C. Belver, Novel isoreticular UiO-66-NH_2 frameworks by N-cycloalkyl functionalization of the 2-aminoterephtalate linker with enhanced solar photocatalytic degradation of acetaminophen, Chem. Eng. J. 461 (2023) 141889, https://doi.org/10.1016/J.CEJ.2023.141889.
[29] I. Papailias, T. Giannakopoulou, N. Todorova, D. Demotikali, T. Vaimakis, C. Trapalis, Effect of processing temperature on structure and photocatalytic properties of g-C_3N_4, Appl. Surf. Sci. 358 (2015) 278–286, https://doi.org/10.1016/J.APSUSC.2015.08.097.
[30] C. Dai, H. Zhang, R. Li, H. Zou, Synthesis and characterization of thiourea, polish journal of, Chem. Technol. 21 (2019) 35–39, https://doi.org/10.2478/PJCT-2019-0027.
[31] V.P. Timchenko, A.L. Novozhilov, O.A. Slepysheva, Kinetics of thermal decomposition of thiourea, Russ. J. Gen. Chem. 74 (2004) 1046–1050, https://doi.org/10.1023/B:RUGC.0000045862.69442.AA.
[32] J. Madarász, G. Pokol, Comparative evolved gas analyses on thermal degradation of thiourea by coupled TG-FTIR and TG/DTA-MS instruments, J. Therm. Anal. Calorim. 88 (2007) 329–336, https://doi.org/10.1007/S10973-006-8058-4.
[33] S. Zhang, G. Li, H. Wang, C. Li, T. Li, Y. Zhang, Study on the pyrolysis of ammonium thiocyanate and its product formation characteristics in H_2, J. Anal. Appl. Pyrolysis 134 (2018) 427–438, https://doi.org/10.1016/J.JAAP.2018.07.009.
[34] N. Rahmanian, S. Naderi, E. Supuk, R. Abbas, A. Hassanpour, Urea finishing process: Prilling versus granulation, Proc. Eng. 102 (2015) 174–181, https://doi.org/10.1016/J.PROENG.2015.01.122.
[35] K. Krum, R. Patil, H. Christensen, H. Hashemi, Z. Wang, S. Li, P. Glarborg, H. Wu, Kinetic modeling of urea decomposition and byproduct formation, Chem. Eng. Sci. 230 (2021) 116138, https://doi.org/10.1016/J.CES.2020.116138.
[36] P.M. Schaber, J. Colson, S. Higgins, D. Thielen, B. Anspach, J. Brauer, Thermal decomposition (pyrolysis) of urea in an open reaction vessel, Thermochim. Acta 424 (2004) 131–142, https://doi.org/10.1016/J.TCA.2004.05.018.
[37] W. Yang, L. Jia, P. Wu, H. Zhai, J. He, C. Liu, W. Jiang, Effect of thermal program on structure–activity relationship of g-C_3N_4 prepared by urea pyrolysis and its application for controllable production of g-C_3N_4, J. Solid State Chem. 304 (2021) 122545, https://doi.org/10.1016/J.JSSC.2021.122545.
[38] F. Fina, S.K. Callear, G.M. Carins, J.T.S. Irvine, Structural investigation of graphitic carbon nitride via XRD and neutron diffraction, Chem. Mater. 27 (2015) 2612–2618, https://doi.org/10.1021/ACS.CHEMMATER.5B00411.
[39] G. Xin, Y. Meng, Pyrolysis synthesized g-C_3N_4 for photocatalytic degradation of methylene blue, J. Chemother. 2013 (2013) 187912, https://doi.org/10.1155/2013/187912.
[40] X. Liu, R. Ma, L. Zhuang, B. Hu, J. Chen, X. Liu, X. Wang, Recent developments of doped g-C_3N_4 photocatalysts for the degradation of organic pollutants, Crit. Rev. Environ. Sci. Technol. 51 (2021) 751–790, https://doi.org/10.1080/10643389.2020.1734433.
[41] F.N. Habarugira, D. Yao, W. Miao, C. Chu, Z. Chen, S. Mao, Synergy of sodium doping and nitrogen defects in carbon nitride for promoted photocatalytic synthesis of hydrogen peroxide, Chin. Chem. Lett. 35 (2024) 109886, https://doi.org/10.1016/J.CCLET.2024.109886.
[42] J. Zhang, S. Hu, Y. Wang, A convenient method to prepare a novel alkali metal sodium doped carbon nitride photocatalyst with a tunable band structure, RSC Adv. 4 (2014) 62912–62919, https://doi.org/10.1039/C4RA11377B.
[43] Pratibha Jigyasa, J.K. Rajput, Alkali metal (Na/ K) doped graphitic carbon nitride (g-C_3N_4) for highly selective and sensitive electrochemical sensing of nitrite in water and food samples, J. Electroanal. Chem. 878 (2020) 114605, https://doi.org/10.1016/J.JELECHEM.2020.114605.
[44] T.S. Miller, A.B. Jorge, T.M. Suter, A. Sella, F. Corà, P.F. McMillan, Carbon nitrides: synthesis and characterization of a new class of functional materials, Phys. Chem. Chem. Phys. 19 (2017) 15613–15638, https://doi.org/10.1039/C7CP02711G.
[45] Z. Ding, X. Chen, M. Antonietti, X. Wang, Synthesis of transition metal-modified carbon nitride polymers for selective hydrocarbon oxidation, ChemSusChem 4 (2011) 274–281, https://doi.org/10.1002/CSSC.201000149.
[46] X. Li, J. Zhang, L. Shen, Y. Ma, W. Lei, Q. Cui, G. Zou, Preparation and characterization of graphitic carbon nitride through pyrolysis of melamine, Appl. Phys. A Mater. Sci. Process. 94 (2009) 387–392, https://doi.org/10.1007/S00339-008-4816-4.
[47] J. Wei, P. Hing, Z.Q. Mo, TEM, XPS and FTIR characterization of sputtered carbon nitride films, Surf. Interface Anal. 28 (1999) 208–211.
[48] D. Zhao, C.-L. Dong, B. Wang, C. Chen, Y.-C. Huang, Z. Diao, S. Li, L. Guo, S. Shen, D. Zhao, B. Wang, Z. Diao, L. Guo, S. Shen, C. Dong, Y. Huang, C. Chen, S. Li, Synergy of dopants and defects in graphitic carbon nitride with exceptionally modulated band structures for efficient photocatalytic oxygen evolution, Adv. Mater. 31 (2019) 1903545, https://doi.org/10.1002/ADMA.201903545.
[49] M. Kim, S. Hwang, J.S. Yu, Novel ordered nanoporous graphitic C_3N_4 as a support for Pt–Ru anode catalyst in direct methanol fuel cell, J. Mater. Chem. 17 (2007) 1656–1659, https://doi.org/10.1039/B702213A.
[50] E. Lieber, C.N.R. Rao, J. Ramachandran, The infrared spectra of organic thiocyanates and isothiocyanates, Spectrochim. Acta 13 (1959) 296–299, https://doi.org/10.1016/0371-1951(59)80030-8.
[51] I. Bertini, A. Sabatini, Infrared spectra of substituted thiocyanate complexes. The effect of the substituent on bond type. II, Inorg. Chem. 5 (1966) 1025–1028, https://doi.org/10.1021/IC50040A017.
[52] M. Thommes, K. Kaneko, A.V. Neimark, J.P. Olivier, F. Rodríguez-Reinoso, J. Rouquerol, K.S.W.W. Sing, Physisorption of gases, with special reference to the evaluation of surface area and pore size distribution (IUPAC technical report), Pure Appl. Chem. 87 (2015) 1051–1069.
[53] L. Kong, J. Wang, X. Mu, R. Li, X. Li, X. Fan, P. Song, F. Ma, M. Sun, Porous size dependent g-C_3N_4 for efficient photocatalysts: regulation synthesizes and physical mechanism, mater today, Energy 13 (2019) 11–21, https://doi.org/10.1016/J.MTENER.2019.04.011.
[54] S. Stefa, M. Zografaki, M. Dimitropoulos, G. Paterakis, C. Galiotis, P. Sangeetha, G. Kiriakidis, M. Konsolakis, V. Binas, High surface area g-C_3N_4 nanosheets as superior solar-light photocatalyst for the degradation of parabens, Appl. Phys. A Mater. Sci. Process. 129 (2023) 1–12, https://doi.org/10.1007/S00339-023-07032-Y.
[55] D.S. Pattanayak, D. Pal, C. Thakur, The influence of various precursors on solar-light-driven g-C_3N_4 synthesis and its effect on photocatalytic tetracycline hydrochloride (TCH) degradation, Inorg. Chem. Commun. 162 (2024) 112201, https://doi.org/10.1016/J.INOCHE.2024.112201.
[56] E. Fernandes, P. Mazierski, T. Klimczuk, A. Zaleska-Medynska, R.C. Martins, J. Gomes, G-C_3N_4 for photocatalytic degradation of parabens: precursors influence, the radiation source and simultaneous ozonation evaluation, Catalysts 13 (2023) 789, https://doi.org/10.3390/CATAL13050789.
[57] Y. Wen, D. Qu, L. An, X. Gao, W. Jiang, D. Wu, D. Yang, Z. Sun, Defective g-C_3N_4 prepared by the $NaBH_4$ reduction for high-performance H_2 production, ACS Sustain. Chem. Eng. 7 (2019) 2343–2349, https://doi.org/10.1021/ACSSUSCHEMENG.8B05124.
[58] M. Smith, L. Scudiero, J. Espinal, J.S. McEwen, M. Garcia-Perez, Improving the deconvolution and interpretation of XPS spectra from chars by ab initio calculations, Carbon N. Y. 110 (2016) 155–171, https://doi.org/10.1016/J.CARBON.2016.09.012.
[59] H. Xu, Z. Wu, Y. Wang, C. Lin, Enhanced visible-light photocatalytic activity from graphene-like boron nitride anchored on graphitic carbon nitride sheets, J. Mater. Sci. 52 (2017) 9477–9490, https://doi.org/10.1007/S10853-017-1167-6.
[60] X. Wang, B. Liu, X. Xiao, S. Wang, W. Huang, Boron dopant simultaneously achieving nanostructure control and electronic structure tuning of graphitic carbon nitride with enhanced photocatalytic activity, J. Mater. Chem. C Mater. 9 (2021) 14876–14884, https://doi.org/10.1039/D1TC04142H.
[61] U. Caudillo-Flores, D. Rodríguez-Padrón, M.J. Muñoz-Batista, A. Kubacka, R. Luque, M. Fernández-García, Facile synthesis of B/g-C_3N_4 composite materials for the continuous-flow selective photo-production of acetone, Green Chem. 22 (2020) 4975–4984, https://doi.org/10.1039/D0GC01326A.
[62] Z.E. Pettifer, J.S. Quinton, S.L. Harmer, Reconstruction of pyrrhotite fracture surfaces, Miner. Eng. 184 (2022) 107666, https://doi.org/10.1016/J.MINENG.2022.107666.
[63] J.G.A. Terlingen, J. Feijen, A.S. Hoffman, Immobilization of surface active compounds on polymer supports using glow discharge processes: 1. Sodium dodecyl sulfate on poly(propylene), J. Colloid Interface Sci. 155 (1993) 55–65, https://doi.org/10.1006/JCIS.1993.1009.
[64] J. Gardella, S.A. Ferguson, R.L. Chin, $\pi^* \leftarrow \pi$ shakeup satellites for the analysis of structure and bonding in aromatic polymers by X-ray photoelectron spectroscopy, Appl. Spectrosc. 40 (1986) 224–232, https://doi.org/10.1366/0003702864509565.
[65] K.L. Wang, Y. Li, T. Sun, F. Mao, J.K. Wu, B. Xue, Fabrication of Na, cl co-doped graphitic carbon nitride with enhanced photocatalytic activity for degradation of dyes and antibiotics, J. Mater. Sci. Mater. Electron. 30 (2019) 4446–4454, https://doi.org/10.1007/S10854-019-00733-2.
[66] J. Liu, T. Zhang, Z. Wang, G. Dawson, W. Chen, Simple pyrolysis of urea into graphitic carbon nitride with recyclable adsorption and photocatalytic activity, J. Mater. Chem. 21 (2011) 14398–14401, https://doi.org/10.1039/C1JM12620B.
[67] N. Chidhambaram, K. Ravichandran, Single step transformation of urea into metal-free g-C_3N_4 nanoflakes for visible light photocatalytic applications, Mater. Lett. 207 (2017) 44–48, https://doi.org/10.1016/J.MATLET.2017.07.040.
[68] S. Panneri, P. Ganguly, B.N. Nair, A.A.P. Mohamed, K.G.K. Warrier, U.N. S. Hareesh, Role of precursors on the photophysical properties of carbon nitride and its application for antibiotic degradation, Environ. Sci. Pollut. Res. 24 (2017) 8609–8618, https://doi.org/10.1007/S11356-017-8538-Z.
[69] K. Sun, J. Shen, Q. Liu, H. Tang, M. Zhang, S. Zulfiqar, C. Lei, Synergistic effect of co(II)-hole and Pt-electron cocatalysts for enhanced photocatalytic hydrogen evolution performance of P-doped g-C_3N_4, Chin. J. Catal. 41 (2020) 72–81, https://doi.org/10.1016/S1872-2067(19)63430-3.
[70] Á. Pérez-Molina, L.M. Pastrana-Martínez, L.T. Pérez-Poyatos, S. Morales-Torres, F. J. Maldonado-Hódar, One-pot thermal synthesis of g-C_3N_4/ZnO composites for the degradation of 5-Fluoruracil cytostatic drug under UV-LED irradiation, Nanomaterials 12 (2022) 340, https://doi.org/10.3390/NANO12030340.
[71] Y. Cui, J. Zhang, G. Zhang, J. Huang, P. Liu, M. Antonietti, X. Wang, Synthesis of bulk and nanoporous carbon nitride polymers from ammonium thiocyanate for

photocatalytic hydrogen evolution, J. Mater. Chem. 21 (2011) 13032–13039, https://doi.org/10.1039/C1JM11961C.
[72] H. Sun, S.J. Park, Phosphorus-doped g-C_3N_4/SnS nanocomposite for efficient photocatalytic reduction of aqueous Cr(VI) under visible light, Appl. Surf. Sci. 531 (2020) 147325, https://doi.org/10.1016/J.APSUSC.2020.147325.
[73] D. Waffel, B. Alkan, Q. Fu, Y.T. Chen, S. Schmidt, C. Schulz, H. Wiggers, M. Muhler, B. Peng, Towards mechanistic understanding of liquid-phase cinnamyl alcohol oxidation with tert-butyl Hydroperoxide over Noble-metal-free $LaCo_{1-x}Fe_xO_3$ perovskites, Chempluschem 84 (2019) 1155–1163, https://doi.org/10.1002/CPLU.201900429.
[74] D. Dvoranová, Z. Barbieriková, V. Brezová, Radical intermediates in photoinduced reactions on TiO_2 (An EPR spin trapping study), Molecules 19 (2014) 17279–17304, https://doi.org/10.3390/MOLECULES191117279.
[75] J. Rivas, R.R. Solis, O. Gimeno, J. Sagasti, Photocatalytic elimination of aqueous 2-methyl-4-chlorophenoxyacetic acid in the presence of commercial and nitrogen-doped TiO2, Int. J. Environ. Sci. Technol. 12 (2015) 513–526, https://doi.org/10.1007/s13762-013-0452-4.
[76] E.M. Rodríguez, G. Márquez, M. Tena, P.M. Álvarez, F.J. Beltrán, Determination of main species involved in the first steps of TiO_2 photocatalytic degradation of organics with the use of scavengers: the case of ofloxacin, Appl. Catal. B 178 (2015) 44–53, https://doi.org/10.1016/j.apcatb.2014.11.002.
[77] P. Zheng, Z. Pan, H. Li, B. Bai, W. Guan, Effect of different type of scavengers on the photocatalytic removal of copper and cyanide in the presence of TiO2@yeast hybrids, J. Mater. Sci. Mater. Electron. 26 (2015) 6399–6410, https://doi.org/10.1007/S10854-015-3229-3/FIGURES/9.
[78] J. Wang, Z. Bian, J. Zhu, H. Li, Ordered mesoporous TiO_2 with exposed (001) facets and enhanced activity in photocatalytic selective oxidation of alcohols, J. Mater. Chem. A Mater. 1 (2012) 1296–1302, https://doi.org/10.1039/C2TA00035K.
[79] S. Garg, A.L. Rose, T.D. Waite, Production of reactive oxygen species on photolysis of dilute aqueous quinone solutions, Photochem. Photobiol. 83 (2007) 904–913, https://doi.org/10.1111/J.1751-1097.2007.00075.X.
[80] A.E. Alegría, A. Ferrer, G. Santiago, E. Sepúlveda, W. Flores, Photochemistry of water-soluble quinones. Production of the hydroxyl radical, singlet oxygen and the superoxide ion, J. Photochem. Photobiol. A Chem. 127 (1999) 57–65, https://doi.org/10.1016/S1010-6030(99)00138-0.
[81] M.S. Alam, B.S.M. Rao, E. Janata, ·OH reactions with aliphatic alcohols: evaluation of kinetics by direct optical absorption measurement. A pulse radiolysis study, Radiat. Phys. Chem. 67 (2003) 723–728, https://doi.org/10.1016/S0969-806X(03)00310-4.
[82] L.L.S. Silva, W. Abdelraheem, M.N. Nadagouda, A.M. Rocco, D.D. Dionysiou, F. V. Fonseca, C.P. Borges, Novel microwave-driven synthesis of hydrophilic polyvinylidene fluoride/polyacrylic acid (PVDF/PAA) membranes and decoration with nano zero-valent-iron (nZVI) for water treatment applications, J. Membr. Sci. 620 (2021) 118817, https://doi.org/10.1016/J.MEMSCI.2020.118817.
[83] B.R. Shah, U.D. Patel, Mechanistic aspects of photocatalytic degradation of Lindane by TiO_2 in the presence of oxalic acid and EDTA as hole-scavengers, J. Environ. Chem. Eng. 9 (2021) 105458, https://doi.org/10.1016/J.JECE.2021.105458.
[84] J. Madona, C. Sridevi, G. Velraj, J. Wu, B. Torsykbayeva, E. Aimbetova, A. Hosseini-Bandegharaei, Boosting solar-driven photocatalytic degradation of organic contaminants and bacterial deactivation using marigold- like Cu_2O decorated g-C_3N_4 nanocomposite, J. Mol. Liq. 403 (2024) 124870, https://doi.org/10.1016/J.MOLLIQ.2024.124870.
[85] C. Bian, Y. Wang, Y. Yi, S. Shao, P. Sun, Y. Xiao, W. Wang, X. Dong, Enhanced photocatalytic activity of S-doped graphitic carbon nitride hollow microspheres: synergistic effect, high-concentration antibiotic elimination and antibacterial behavior, J. Colloid Interface Sci. 643 (2023) 256–266, https://doi.org/10.1016/J.JCIS.2023.04.034.
[86] S. Shao, X. Liu, R. Wang, Y. He, C. Bian, P. Sun, X. Dong, Morphologic and microstructural modulation of graphitic carbon nitride through EDTA-2Na mediated supramolecular self-assembly route: enhanced visible-light-driven photocatalytic activity for antibiotic degradation, Appl. Surf. Sci. 669 (2024) 160501, https://doi.org/10.1016/J.APSUSC.2024.160501.
[87] W. Chen, Z. Chen, T. Liu, Z. Jia, X. Liu, Fabrication of highly visible light sensitive graphite-like C_3N_4 hybridized with $Zn_{0.28}Cd_{0.72}S$ heterojunctions photocatalyst for degradation of organic pollutants, J. Environ. Chem. Eng. 2 (2014) 1889–1897, https://doi.org/10.1016/J.JECE.2014.07.019.
[88] J. Cao, W. Nie, L. Huang, Y. Ding, K. Lv, H. Tang, Photocatalytic activation of sulfite by nitrogen vacancy modified graphitic carbon nitride for efficient degradation of carbamazepine, Appl. Catal. B 241 (2019) 18–27, https://doi.org/10.1016/J.APCATB.2018.09.007.
[89] F. Yang, M. Lublow, S. Orthmann, C. Merschjann, T. Tyborski, M. Rusu, S. Kubala, A. Thomas, R. Arrigo, M. Hävecker, T. Schedel-Niedrig, Metal-free photocatalytic graphitic carbon nitride on p-type chalcopyrite as a composite photocathode for light-induced hydrogen evolution, ChemSusChem 5 (2012) 1227–1232, https://doi.org/10.1002/CSSC.201100691.
[90] T. Gao, D. Zhao, S. Yuan, M. Zheng, X. Pu, L. Tang, Z. Lei, Energy band engineering of graphitic carbon nitride for photocatalytic hydrogen peroxide production, carbon, Energy (2024) e596, https://doi.org/10.1002/CEY2.596.
[91] W.H. Koppenol, D.M. Stanbury, P.L. Bounds, Electrode potentials of partially reduced oxygen species, from dioxygen to water, Free Radic. Biol. Med. 49 (2010) 317–322, https://doi.org/10.1016/J.FREERADBIOMED.2010.04.011.
[92] P.M. Wood, The potential diagram for oxygen at pH 7, Biochem. J. 253 (1988) 287–289, https://doi.org/10.1042/BJ2530287.